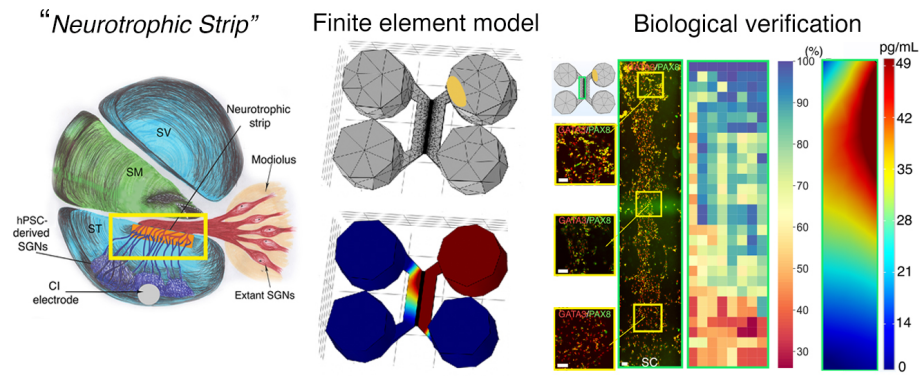


Graphical Abstract

Developing the Bioactive Cochlear Implant: Bridging the electrode–neuron gap through neurite guidance

Kevin T. Nella, Benjamin M. Norton, Hsiang-Tsun Chang, Rachel A. Heuer,
Christian B. Roque, Akihiro J. Matsuoka



Developing the Bioactive Cochlear Implant: Bridging the electrode–neuron gap through neurite guidance

Kevin T. Nella^{a,b}, Benjamin M. Norton^a, Hsiang-Tsun Chang^a, Rachel A. Heuer^a, Christian B. Roque^a, Akihiro J. Matsuoka^{a,c,d,e,*}

^a*Department of Otolaryngology–Head and Neck Surgery, Feinberg School of Medicine, Northwestern University, Chicago IL, 60611, USA*

^b*Department of Mechanical Engineering, Robert R. McCormick School of Engineering and Applied Science, Northwestern University, Evanston, IL., USA*

^c*Simpson Querrey Institute, Chicago IL, 60611, USA*

^d*Roxelyn and Richard Pepper Department of Communication Sciences and Disorders, School of Communication, Northwestern University, Evanston, IL., 60210, USA*

^e*The Hugh Knowles Center for Clinical and Basic Science in Hearing and its Disorders, Evanston, IL. 60210, USA*

Abstract

Although cochlear implant (CI) technology has allowed partial restoration of hearing over the last few decades, persistent challenges remain - including the deciphering of rich acoustic signals into a digital pulse-train signal. Among these challenges, the “electrode–neuron gap” poses the most significant obstacle to advancing past the current plateau in CI performance. Resulting issues include limited performance in noisy environments and a poor ability to decode intonation and music. We propose the development of the “neuroregenerative nexus”—a biological interface that doubly preserves endogenous spiral ganglion neurons (SGNs) while precisely directing the growth of neurites arising from transplanted human pluripotent stem cell (hPSC)-derived otic neuronal progenitors (ONPS), toward endogenous SGNs. We hypothesized that the Polyhedrin Delivery System (PODS®-human brain-derived neurotrophic

*Corresponding author: Akihiro J. Matsuoka, Department of Otolaryngology–Head and Neck Surgery, Feinberg School of Medicine, Northwestern University, 676 North St. Clair Street Suite 1325, Chicago, IL 60611, USA. E-mail addresses: amatsuok@nm.org, akihiro.matsuoka@northwestern.edu.

Email addresses: kevin.nella@northwestern.edu (Kevin T. Nella), benjamin.norton@northwestern.edu (Benjamin M. Norton), hsiangtsun.chang@gmail.com (Hsiang-Tsun Chang), racheuer@gmail.com (Rachel A. Heuer), christian.b.roq@gmail.com (Christian B. Roque), amatsuok@nm.org (Akihiro J. Matsuoka)

factor [BDNF]) could stably provide an adequate BDNF gradient to hPSC-derived ONPs, thereby simultaneously facilitating otic neuronal differentiation and directional neurite outgrowth. To test this hypothesis, we first devised a finite element model to simulate the *in vitro* BDNF gradient generated by PODS®. For biological verification, we validated the concept of the neuroregenerative nexus by using a multi-chamber microfluidic device, which mimics the *in vivo* micro-environment more accurately than conventional laboratory plates in terms of volume and concentrations of endogenous/exogenous factors. We were able to generate the optimal BDNF concentration gradient to enable survival, neuronal differentiation toward hPSC-derived SGNs, and directed neurite extension of hPSC-derived SGNs. The technique will allow us to further advance our concept of the “neuroregenerative nexus” by controlling neurite direction of transplanted hPSC-derived ONPs. This proof-of-concept study provides a step toward the next generation of CI technology.

Keywords: human pluripotent stem cells, finite element model, microfluidic device, neurotrophic factor, cochlear implant, neuroelectric interface, stem cell niche, spiral ganglion neurons

2010 MSC: 74S05, 62P10, 92C20

¹ **1. Introduction**

² The cochlear implant (CI), which provides functional restoration in patients
³ with sensorineural hearing loss, forms a neuro-electronic interface with the pe-
⁴ ripheral auditory nervous system [1]. CI technology functions by electrically
⁵ stimulating the extant population of auditory neurons (i.e., spiral ganglion neu-
⁶ rons [SGNs]). Although CI technology has allowed partial restoration of hearing
⁷ for this patient population over the last few decades, persistent challenges, in-
⁸ cluding the deciphering of rich acoustic signals into digital pulse-train signals,
⁹ remain. Among these challenges, the “electrode-neuron gap” poses the most
¹⁰ significant obstacle to advancing past the current plateau in CI performance.
¹¹ This phenomenon symptomatically manifests as limited performance in noisy
¹² environments and poor ability to decode intonation and music [2], arguably de-
¹³ creasing quality of life. The gap exists between the CI electrode and the target
¹⁴ membranes of dendrites in surviving endogenous SGNs [3]. It results in the
¹⁵ requirement of larger CI excitation fields, leading to current spread that excites
¹⁶ and therefore disables the neighboring electrodes, resulting in fewer information
¹⁷ channels to the brain, all within discrete time steps [2, 4]. This can develop into
¹⁸ a vicious cycle as fewer information channels to the brain also prompt the need
¹⁹ for larger CI excitation fields. The length of the gap generally spans hundreds of
²⁰ μm [5, 6]. Hahnewald et al. demonstrated *in vitro* that energy needed to elicit
²¹ a response can be reduced by up to 20% by reducing the distance from 40 to
²² zero μm (by growing early postnatal mouse SGN explants on a microelectrode
²³ array) [4].

²⁴ Previous work has introduced the concept of a “bioactive” CI to resolve the
²⁵ electrode-neuron gap *in vivo*[7, 8, 9]. The bioactive CI combines the current
²⁶ state-of-the-art CI technology with emerging stem cell-replacement therapy in
²⁷ the inner ear. In this scheme, transplanted human pluripotent stem cell (hPSC)-
²⁸ derived SGNs bridge the gap between the CI electrode and surviving endogenous
²⁹ SGNs. Furthermore, introducing neurotrophin gradients has been shown to
³⁰ guide hPSC grafts in spinal cord injury [10], direct growth of endogenous SGNs

31 toward CI electrodes in the scala tympani [11], and enable transplanted hPSC
32 derived otic neuronal progenitors (ONPs) to grow neurites toward the modio-
33 lus [9]. Although promising, these studies failed to observe adequate directed
34 neurite outgrowth toward endogenous SGNs (i.e., lack of synaptic connections
35 between hPSC grafts and endogenous SGNs), presumably preventing significant
36 improvements in functional recovery of hearing.

37 To confront this issue, we propose the development of a “neurotrophic strip”—a
38 biological interface that doubly preserves endogenous SGNs and precisely directs
39 the growth of neurites arising from transplanted hPSC-derived ONPs toward
40 the endogenous SGNs. The highlighted yellow-square area in Figure 1A shows
41 a schematic diagram of this concept. Here, the neurotrophic strip (shown as
42 an orange rectangle in Figure 1A) stimulates neurite outgrowth from both the
43 hPSC-derived ONPs and the endogenous SGNs via a neurotrophic factor gra-
44 dient [12]. While the concept of using a neurotrophin gradient for directional
45 axonal growth has existed for a few decades, incorporation of neurotrophin gra-
46 dients with any tissue- or bio-engineered scaffold has been extremely challenging
47 due to the lack of self-sustaining neurotrophin delivery methods—their eventual
48 depletion triggers an accelerated decline in neurite growth and survival of extant
49 SGNs [13, 14, 15]. One major contributor is the structurally unstable nature of
50 neurotrophins, which suffer from fragility and thermo-instability under normal
51 physiological conditions both *in vitro* and *in vivo*, leading to short half-lives
52 typically ranging from minutes to hours [16]. We set out to mitigate this phe-
53 nomenon by utilizing the polyhedrin delivery system (PODS®)—a crystalline
54 growth factor formulation developed to enable long-term release of growth fac-
55 tors (e.g., neurotrophins) [17, 18, 19] (Figure 1B). The PODS® technology has
56 adapted viral machinery to encase a chosen growth factor into polyhedrin pro-
57 tein cases. The resultant growth factor co-crystals have slow degradation profiles
58 under physiological conditions and, therefore, allow the sustained release of em-
59 bedded bioactive growth factors.

60 We reasoned that a bio-engineered scaffolding incorporated with PODS®
61 technology can establish a neuronal network between transplanted hPSC-derived

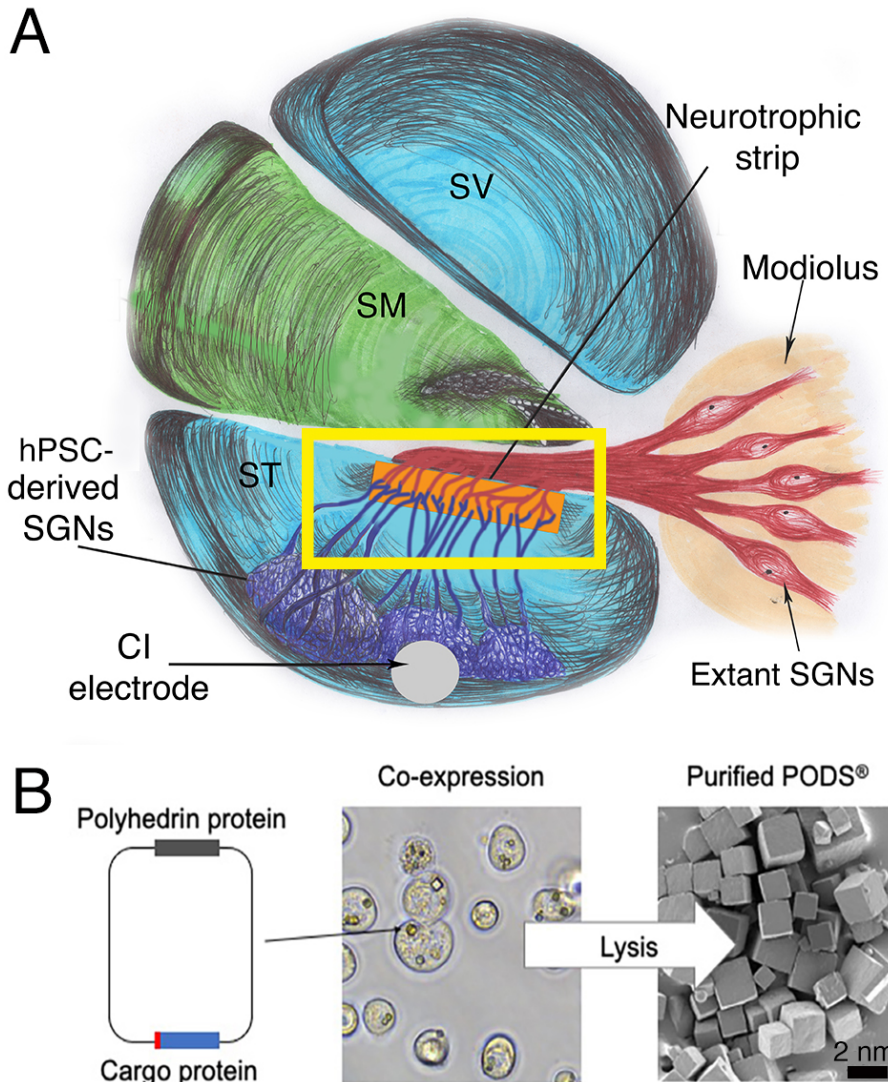


Figure 1: (A): A next-generation bioactive CI and a neurotrophic strip. The neural network in this scheme consists of a CI electrode, transplanted stem cell-derived SGNs, the neurotrophic strip, and extant/endogenous SGNs (red). Note that neuronal connection is largely absent with hair cells (not shown). (B): Polyhedrin Delivery System (PODS)®. PODS® crystals are cubic protein co-crystals produced by Sf9 cells (a clonal isolate of *Spodoptera frugiperda* Sf21 cells [IPLB-Sf21-AE], in which the polyhedrin protein and a second protein are co-expressed). This second protein is termed as the active, or cargo protein (Figure 1B, left). Inside the Sf9 cells, polyhedrin proteins self-assemble into cubic crystals (Figure 1B, center) while the active protein, tagged with a short peptide sequence, binds to the growing polyhedrin crystal. The crystals are extracted and purified by simple cell lysis and washes to remove cell debris (Scanning electron micrograph, Figure 1B, right).

62 ONP grafts and extant SGNs in the inner ear. More specifically, we hypothe-
63 sized that PODS®-recombinant human neurotrophin system could stably pro-
64 vide and maintain an adequate neurotrophin gradient to facilitate otic neuronal
65 differentiation of and directional neurite outgrowth from hPSC-derived ONPs, .
66 To test this hypothesis, we first devised a finite element model (FEM) to simu-
67 late the *in vitro* neurotrophin gradient generated by PODS®. In this study, we
68 focus on the role of BDNF—the most studied of the neurotrophins in the inner
69 ear, and the most vital for the functional recovery of damaged SGNs [20]. For
70 biological validation and demonstration we used a multi-chamber microfluidic
71 device, that which mimics the *in vivo* micro-environment of the inner ear more
72 so than conventional laboratory plates in terms of volume and concentrations
73 of endogenous/exogenous factors [21].

74 **2. Materials and Methods**

75 *2.1. Polyhedrin delivery system*

76 The Polyhedrin Delivery System (PODS®-human BDNF [rhBDNF]) (Cell
77 Guidance Systems, Cambridge, United Kingdom) was used as a self sustain-
78 ing source of rhBDNF. PODS®-rhBDNF is composed of the polyhedrin pro-
79 tein formed by *Bombyx mori*, an insect from the moth family *Bombycidae*. A
80 cargo protein (i.e., rhBDNF) is co-expressed within the polyhedrin crystal and is
81 slowly released by breakdown of the PODS® crystals via cell-secreted proteases
82 (Figure 1B)[9, 18, 22].

83 *2.2. Human pluripotent stem cell culture using dual-compartment microfluidic
84 device*

85 Human embryonic stem cells (hESCs: H7 and H9, passages number 25–35)
86 and were obtained from WiCell Research Institute (Madison, Wisconsin, USA).
87 Human induced pluripotent stem cells (hiPSCs: TC-1133HKK, passage num-
88 ber 22–35) were generated from human CD34+ cord blood cells using the four
89 Yamanaka factors at Lonza (Walkersville, Maryland [MD], USA). The hiPSC

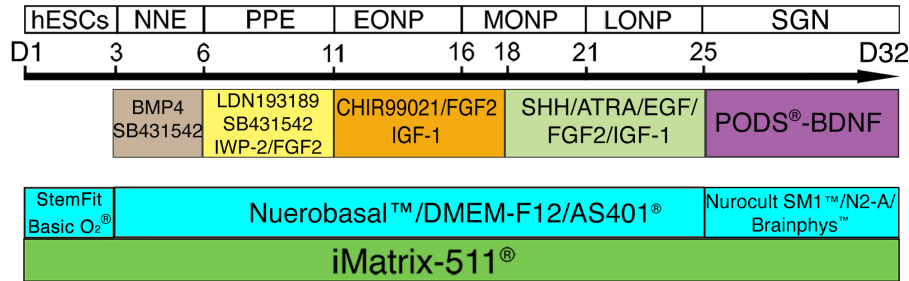


Figure 2: Overview of otic neuronal differentiation protocol for hPSCs. Please see detail in [8, 9, 23, 24] and the Supplemental Data. Each developmental stage is shown at the top, with key treatments shown below. NNE: nonneuronal ectoderm; PPE: preplacodal ectoderm; EONP: early-stage otic neuronal progenitor; MONP: mid-stage otic neuronal progenitor; LONP: late-stage otic neuronal progenitor; BMP4: bone morphogenetic protein 4; SHH: Sonic hedgehog; ATRA: all-trans retinoic acid; EGF: epidermal growth factor; IGF-1: insulin-like growth factor-1; FGF2: fibroblast growth factor 2; N2B27-CDM: chemically defined medium containing N2 and B27 supplements.

90 cell line (TC-1133HKK) was kindly provided by Healios K.K. (Tokyo, Japan).
 91 hPSC-derived ONPs were derived based on our previously established protocol
 92 (Supplemental Data) [8, 9, 23, 24]. A step-wise series of ligands and growth
 93 factors was added to a neuronal induction medium to promote hPSC differen-
 94 tiation toward the late-stage ONP lineage—mitotic progenitor population that
 95 generates the SGNs. (Figure 2).

96 Microfluidic devices provide a platform for specifically evaluating axonal re-
 97 generation [25]. Here, multi-chamber microfluidic devices, Xona™ Microfluidics
 98 XC150 and XC450 (Xona™ Microfluidics, Research Triangle Park, North Car-
 99 olina, USA), were used for computational calculation and biological validation
 100 (Figure 3A–B) of an FEA. The Xona™ device allows for neurites to grow to-
 101 ward growth factors in the opposite chamber while limiting migration of derived
 102 ONP cell bodies due to specific dimensions of the device. Additionally, the mi-
 103 crochannel array between the two chambers mimics the porous bony separation
 104 (osseous spiral lamina) between the modiolus (where extant SGNs are localized)
 105 and the scala tympani (where the biohybrid CI will be implanted). Thus the

106 diffusion profile of the released rhBDNF *in vitro* more accurately predicts that
107 of the *in vivo*.

108 The devices were washed and coated with poly-L-ornithine (PLO, 20 μ g/mL
109 in H₂O, Sigma-Aldrich, St. Louis, Missouri [MO], USA) and recombinant
110 laminin-511 (iMatrix-511, 0.5 mg/mL, Nacalai USA, San Diego, California [CA],
111 USA) according to the manufacturer-outlined protocol. Next, approximately
112 1.75 x 10⁵ cells (in 20 μ L of media) were added through the top and bottom left
113 wells into the somal compartment (i.e., total amount of 3.5 x 10⁵ hPSC-derived
114 ONPs were added).

115 PODS®-rhBDNF were placed in the top right well of the neurotrophin com-
116 partment (Figure 3A–B) to generate a rhBDNF concentration gradient to pro-
117 mote directional neurite growth. hPSC-derived ONPs were cultured for 7 days
118 in the Xona™ device to induce otic neuronal differentiation. Note that high-
119 density cell cultures were induced to facilitate molecular studies as well as the
120 generation of a more biologically relevant neuronal phenotype (i.e., otic lineage)
121 [25]. Media was topped off daily after imaging (from 20-40 μ L per well).

122 *2.3. Enzyme-linked immunosorbent assay for brain-derived neurotrophic factor*

123 In order to determine the breakdown and release kinetics of PODS®-rhBDNF,
124 an experiment measuring rhBDNF concentrations at sequential time points was
125 performed. The culture media from both a control and experimental condition
126 were collected at each time point and immediately stored at -80°C before run-
127 ning an enzyme-linked immunosorbent assay (ELISA) after the final collection.
128 The same method was applied to measure the degradation kinetics of rhBDNF
129 protein with a carrier protein (Bovine Serum Albumin [BSA]) (#248-BDB-050,
130 R&D Systems, Minneapolis, Minnesota, USA). Experimental conditions were
131 culture media enriched with 10% fetal bovine serum (FBS) (Thermo Fisher
132 Scientific, Waltham, MA, USA). All rhBDNF samples were quantified with a
133 BDNF ELISA kit (# BGK23560; PeproTech, Rocky Hill, New Jersey, USA),
134 and the results were analyzed with a Synergy HTX Multi-Mode Reader (BioTek,
135 Winocski, Vermont, USA) at a 450 nm wavelength, as instructed by the man-

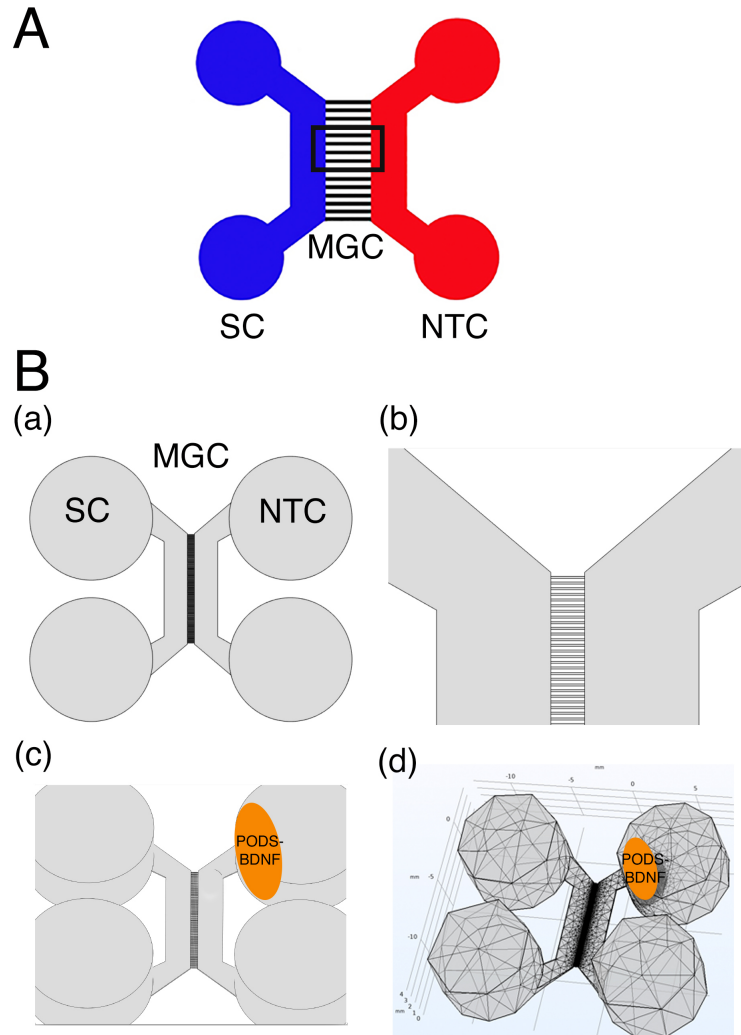


Figure 3: (A): Schematic specification of a XonaTM Microfluidics XC 450. Two main channels (somal compartment (SC) and neurotrophin compartment (NTC)) on either side are connected by a micro-groove channel (MGC) spanning 450 μm with a width of 10 μm (black square). The somal compartment contains hPSC-derived late-stage ONPs (shown in black), while the neurotrophin compartment contains the secreted factors (i.e., BDNF) that are released from PODS®-rhBDNF crystals. (B):(a) XonaTM Microfluidics XC450 device geometry, created at a 1:1 scale with Autodesk Inventor®, in which the diffusion profile of the released BDNF was modeled. (b) Detail of the microchannels adjoining the two compartments of the XonaTM Microfluidics XC450. (c) XonaTM Microfluidics XC450 device showing the optimal area and geometry to localize PODS®-rhBDNF (yellow ellipsoid area). (d): Mesh geometry of the XonaTM XC450 generated with Autodesk Inventor, depicting the localized volume of PODS®-rhBDNF (1 μL) as an ellipsoid disc.

¹³⁶ ufacturer. Molecular kinetics were then calculated using the MATLAB Curve
¹³⁷ Fitting Toolbox (MathWorks, Natick, CA, USA).

¹³⁸ *2.4. Sodium dodecyl sulphate-polyacrylamide gel electrophoresis*

¹³⁹ Sodium dodecyl-sulfate polyacrylamide gel electrophoresis (SDS-PAGE) is
¹⁴⁰ commonly used as a method to separate proteins with molecular masses between
¹⁴¹ 5 and 250 kDa [26], a range of which is suitable for detecting recombinant hu-
¹⁴² man BDNF (molecular weight [MW]: 14kDa [27]) and polyhedrin (MW: ~29
¹⁴³ kDa [22]). In this study, SDS-PAGE was used to assess the molar ratio of poly-
¹⁴⁴ hedrin to BDNF at different quantities. Briefly, each protein sample was diluted
¹⁴⁵ in deionized water and mixed with 6x Laemmli sample buffer (Bio-Rad Labora-
¹⁴⁶ tories, Inc., Des Plaines, Illinois [IL], USA) containing 2-mercaptoethanol and
¹⁴⁷ heated at 100°C for 5 to 20 minutes. Samples were then loaded into precast
¹⁴⁸ Mini-PROTEAN TGX 4-15% polyacrylamide mini-gels (Bio-Rad Laboratories,
¹⁴⁹ Inc., Des Plaines, IL, USA). Then, 5 mL of Precision Plus Protein Kaleido-
¹⁵⁰ scope Prestained Protein Standards (Bio-Rad Laboratories, Inc., Des Plaines,
¹⁵¹ IL, USA) were loaded in each gel run. Electrophoresis was performed at room
¹⁵² temperature for approximately 90 minutes using a constant voltage (100V) in
¹⁵³ 1x solution of Tris-Glycine-SDS electrophoresis buffer (Bio-Rad Laboratories,
¹⁵⁴ Inc., Des Plaines, IL, USA) until the dye front reached the end of the 60 mm
¹⁵⁵ gel. After electrophoresis, the mini-gels were rinsed with deionized water 3
¹⁵⁶ times for 5 minutes and were subsequently incubated in SimplyBlue™ SafeStain
¹⁵⁷ (ThermoFisher Scientific, Waltham, MA, USA) for one hour at room temper-
¹⁵⁸ ature with gently agitation. Images obtained from gels were analyzed using
¹⁵⁹ ImageJ 1.53g (December 4, 2020, the National Institutes of Health, Bethesda,
¹⁶⁰ MD, USA [28]). The calculated molar ratio was applied to the COMSOL®
¹⁶¹ Multiphysics model to accurately predict the amount of rhBDNF released from
¹⁶² PODS®-rhBDNF. SDS-PAGE was performed according to the manufacturer's
¹⁶³ technical guide (Bio-Rad Laboratories, Inc., Des Plaines, IL, USA).

164 *2.5. Western Blot*

165 The identity of the rhBDNF protein detected by SDS-PAGE was verified
166 by western blot (Bio-Rad Laboratories, Inc., Des Plaines, IL, USA). Briefly,
167 the polyvinylidene difluoride (PVDF) membrane was prepared in methanol for
168 30 seconds before soaking in 1x Tris-Glycine-Methanol transfer buffer for 10
169 minutes. Wet transfer was performed at 4°C for approximately 60 minutes us-
170 ing a constant voltage (100V) in 1X solution of Tris-Glycine-Methanol transfer
171 buffer. After transfer, the membrane was briefly rinsed with 1X Tris-buffered
172 saline Tween-20 (TBST) and was subsequently blocked in 5% BSA in TBST for
173 24 hours at 4°C with gentle agitation. The membrane was then rinsed with 1x
174 TBST before incubating in BDNF polyclonal antibody (ThermoFisher Scien-
175 tific, Waltham, MA, USA) diluted to 1:1500 in 1% BSA in TBST for 24 hours at
176 4°C with gentle agitation. Following incubation, the membrane was rinsed in 1x
177 TBST 5 times for 5 minutes to remove unbound primary antibody. Then, the
178 membrane was incubated in Goat anti-Rabbit IgG (H+L) horseradish peroxi-
179 dase (HRP) conjugated secondary antibody (ThermoFisher Scientific, Waltham,
180 MA, USA) diluted to 1:5000 in 1% BSA in TBST for one hour at room tem-
181 perature with gentle agitation. Following incubation, the membrane was rinsed
182 in 1x TBST 5 times for 5 minutes to remove unbound secondary antibody. For
183 sensitive detection, the membrane was treated with Pierce™ ECL Western Blot-
184 ting Substrate (ThermoFisher Scientific, Waltham, MA, USA), and visualized
185 using an Azure 600 Digital Imager (Azure Biosystems, Dublin, CA, USA). Elec-
186 trophoresis buffer for sample condition and run condition was summarized in
187 Supplementary Table S1.

188 *2.6. Three-dimensional finite element analysis*

189 We used finite element analysis (FEA) to simulate the BDNF concentration
190 gradient over time in a multi-chamber microfluidic device. FEA is a compu-
191 tational numerical technique, which approximates mathematical solutions to
192 partial differential equations (PDEs) that appropriately simulate complex real-
193 world problems including stress/strain testing, thermal conduction, and diffu-

194 sion in various geometries and materials. In this study, the FEM allowed us to
195 predict the concentration gradient with respect to time depending on the num-
196 ber of PODS®-rhBDNF introduced into the system. To solve the FEM, we used
197 COMSOL® Multiphysics (version 5.6 [released on November 11, 2020], COM-
198 SOL, Inc., Burlington, Massachusetts [MA], USA), which is a finite element
199 method solution tool for engineering and scientific research computations. We
200 used sustained-release kinetics for PODS®-rhBDNF determined from aforemen-
201 tioned ELISA studies, SDS-PAGE, as well as data from a previous study from
202 our group [9]. Device geometry was generated at a 1:1 scale using Autodesk®
203 Inventor 2019.0.2 (Autodesk, Mill Valley, CA, USA) (Figure 3B). The com-
204 putational analysis was implemented on a high-performance desktop computer
205 platform equipped with a 64 GB RAM CPU (AMD Ryzen Threadripper 3990X
206 64-Core, 128-Thread @ 4.3 GHz) and two GPU cards (NVIDIA GeForce RTX
207 3080Ti, 12GB 384-bit GFF6X Graphics card).

208 *2.7. Immunocytochemistry and image acquisition*

209 Microfluidic devices were coated with poly-d-lysine (PDL) (#A3890401,
210 ThermoFisher Scientific, Waltham, MA, USA) and poly-ornithine (PLO) (#
211 A-004-C, MilliporeSigma, St. Louis, MO, USA) as per the manufacturer's in-
212 structions. A total of 100,000 dissociated hPSC-derived ONPs were plated into
213 the somal compartment of the device. On Day 7, 4% (w/v) paraformaldehyde
214 (PFA) (ThermoFisher Scientific, Waltham, MA, USA) was added to the com-
215 partments for 20 minutes to fix the cells. ICC was used to stain for GATA3,
216 PAX8, and beta-III tubulin. These three proteins have shown to appropriately
217 characterize ONPs in our previous studies [8, 9, 24]. Following PBS wash, cul-
218 tures were blocked with 5% BSA at room temperature for 1 hour. Cultures
219 were then incubated overnight at 4°C on a shaker plate in primary antibody
220 solution using Rabbit anti-Beta-III-Tubulin (1:100, Abcam, Cambridge, MA,
221 USA), Goat anti-PAX8 (1:500, Abcam, Cambridge, MA, USA), and Mouse
222 anti-GATA3 (1:500, R&D Systems, Minneapolis, MN, USA). Following PBS
223 washes, cultures were incubated at room temperature for 90 minutes on a

shaker plate in secondary antibody solution composed of Alexafluor647 anti-Rabbit (1:1000, ThermoFisher Scientific, St. Louis, MO, USA), Alexafluor488 anti-Goat (1:1000, ThermoFisher Scientific, St. Louis, MO, USA), and Alexafluor594 anti-Mouse (1:1000, ThermoFisher Scientific, St. Louis, MO, USA) in 1% BSA. Following PBS -/- washes, cultures were incubated with DAPI for 20 minutes (300 nM, ThermoFisher Scientific, St. Louis, MO, USA). Secondary antibody controls were performed each time multiple primary antibodies were used [29]. Labeling controls (detection controls) were performed for a sample from each batch of hPSC culture [29]. See Supplementary Figure S1 for exemplary figures for these control conditions. Results were imaged using a Nikon Ti2 Widefield Laser Microscope System (Nikon, Tokyo, Japan). Phase-contrast images were captured on a Nikon Eclipse TE2000-U inverted microscope (Nikon, Tokyo, Japan). All fluorescence images were acquired on a Zeiss LSM 510 META laser-scanning confocal microscope (Carl Zeiss, Oberkochen, Germany), a Nikon Ti2 laser scanning confocal microscope (Nikon, Tokyo, Japan), or a Leica SP5 laser-scanning confocal microscope (Leica, Welzlar, Germany). Observers were blinded to the conditions during imaging and tracing. In general, the images were processed with a Image J ver. 1.53j or Matlab R2020b. Further detail on image acquisition and quantification of fluorescent-positive cells can be found in the Supplemental Data.

2.8. Preferred cell orientation analysis

Collective cell migration, where cells organized in a tightly connected fashion migrate as cohesive structures, is a critical biological process to highlight the neurotrophin diffusion profile [30]. To evaluate this process, time-lapse acquisition of images of the Xona™ device was performed using an inverted microscope (Nikon Eclipse TS100, Tokyo, Japan) at Day 1, 3, 5, and 7. Due to the high cell density required for hPSC-ONPs to survive in the somal compartment of the Xona™ device, images were not amenable to manual analysis in most of the cases. To circumvent this problem, we performed a series of image pre-processings that are mainly based on modified binarization-based extraction of

aliment score methods with some modifications [31]. We used MATLAB Image Processing Toolbox R2020b (version 9.9.0.1495850, September 30th, 2020, Mathworks, Natick, MA) for analysis. Please see Supplementary Figure S2 for further detail. The analysis of directional data in general represents a particular challenge: there is no reason to designate any particular point on the circle as zero, and it is somewhat arbitrary depending on where one sets a coordinate [32, 33]. In this study, we used polar coordinates to determine the directionality of preferred cell orientation. For this analysis, we again used MATLAB Image Processing Toolbox R2020b. See detailed discussion on how we determined the preferred cell orientation in Supplementary Figure S3.

2.9. Neurite alignment vector assay, neurite growth assay and cell migration assay

The microfluidic device allowed us to culture hPSC-derived ONPs in a polarized manner and to directly isolate/analyze neurites. To evaluate the neurite projection into the neurotrophin compartment by derived otic neurons cultured in the somal compartment, we performed a neurite alignment vector assay. We also evaluated the length of neurites that grew from hPSC-derived ONPs. For these purposes, hPSC-derived ONPs were cultured in a Xona™ XC450 for seven days and then immunostained with *beta*-III tubulin and DAPI. We used two ImageJ plug-in toolkits, NeuriteTracer and NeuronJ, to assess neurite alignment and neurite growth [34, 35]. Due to the bipolar nature of hPSC-derived ONPs/SGNs, we measured the two longest neurites from the cells [24, 36]. Please see Supplementary Figure S4 for detailed description of this analysis. We used hPSC-derived ONPs cultured with 800,000 PODS®-rhBDNF as a positive control. The quantity 800,000 was chosen based on our FEM in that there was no neurotrophin gradient in the somal compartment. As a negative control, we used 20 ng/mL of recombinant human BDNF. To evaluate cell migration across the microgroove channels, we performed cell migration analysis. We manually counted the number of ONPs that migrated from the somal compartment into the microchannels and neurotrophin compartment.

284 *2.10. Statistical analysis*

285 When appropriate, and as indicated in each figure, statistical analysis was
286 performed. Experimental values are typically expressed as mean and standard
287 error (SE). The majority of the statistical analyses were performed with Python
288 3.9.6. (Python Software Foundation, Wilmington, Delaware, USA). The follow-
289 ing libraries were used for the statistical analysis: Scipy, Numpy, Matplotlib,
290 and Seaborn [37, 38, 39]. Normal distributions were assumed unless mentioned
291 otherwise. *P* values smaller than 0.05 were considered statistically significant.
292 For circular statistics, we derived the sample mean vector and its polar coor-
293 dinate. Mean and confidence intervals were calculated. We chose confidence
294 coefficient, *Q*, e.g. *Q* = 0.95. To analyze the axial nature of data, especially to
295 compute the mean vector angle, we doubled each angle and reduced the mul-
296 tiples modulo 360°. Please see detailed discussion in Supplementary Figure S3
297 and S5. The Rayleigh test of uniformity and V-test were performed to deter-
298 mine whether the samples differ significantly from randomness (i.e., where there
299 is statistical evidence of directionality). One-sample test for the mean angle was
300 performed to test whether the population mean angle is statistically different
301 from the given angle. In all of our circular statistics, von Mises distribution was
302 assumed and also verified. Circular statistics were performed using CircStat: A
303 MATLAB Toolbox [33, 40]. Please see detailed description of circular statistics
304 in Supplementary Figure S3 and S5. Experiments were done in three biological
305 replicates unless otherwise specified in Figure captions.

306 **3. Results**

The appropriate number of PODS®-rhBDNF crystals to induce an effective neurotrophin gradient for otic neuronal differentiation and directed neurite outgrowth was calculated using a three-dimensional FEA that predicts the concentration profile of BDNF formed through the gradual release and diffusion of BDNF from PODS®-rhBDNF. First, we quantified the chemical kinetics of this phenomenon with ELISA testing (Figure 4) to establish the parameters for

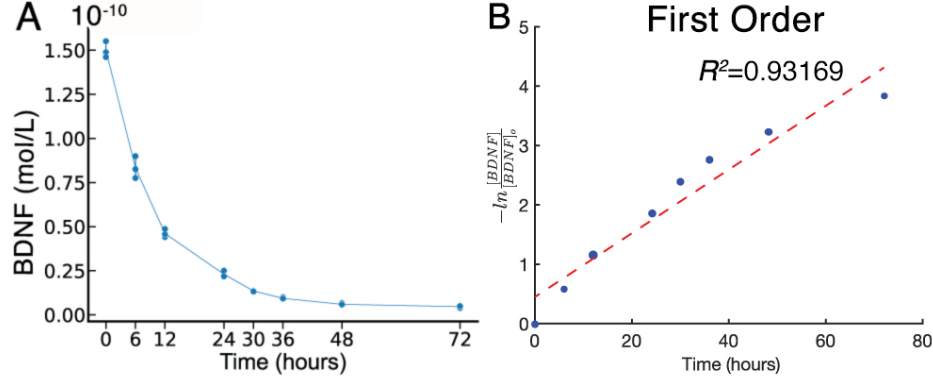
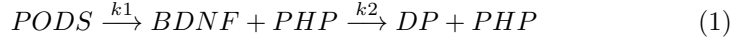


Figure 4: Chemical kinetics of Brain Derived Neurotrophic Factor (BDNF). (A): Concentration of rhBDNF in solution over 72 hours after initial application. (B): $\frac{1}{[BDNF]}$ data fit to first order curve. Please see other curve fit data in Supplemental Figure 1. Red line: fitted line, blue dots: individual data point. k_2 is defined as slope of fitted curve.

the FEA. Here, two consecutive chemical reactions occur: 1) the breakdown of PODS® crystals into polyhedrin protein and rhBDNF, and 2) the degradation of rhBDNF toward the degradation product (Equation (1)).



where DP is the degradation product of the released rhBDNF, PHP is the polyhedrin protein, and k_1 and k_2 are the rate constants ($\frac{1}{hour}$) for their respective reactions.

Degradation kinetics data for rhBDNF was collected while monitoring rhBDNF concentration after introducing a predefined amount into a single well of solution. The data obtained throughout the first 72 hours indicate an exponential decay, suggesting first order kinetics (Figure 4). To confirm this notion, we performed a linear and nonlinear least square analysis of the kinetic data with the MATLAB Curve Fitting Toolbox. We found that the corresponding R^2 was 0.93169 for the first order curve-fit, confirming that the degradation kinetics was indeed first order. The rate constant for a first order reaction is defined to be slope of the time plot of the logarithmic ratio between concentration and

319 initial concentration. The value for k_2 ($0.0679 (\frac{1}{hour})$) is the slope of the loga-
320 rithm of the ratio between concentration and initial concentration (See further
321 detail in Supplementary Figure S7). Furthermore, data for the complete chemi-
322 cal reaction were collected by similarly monitoring rhBDNF concentration over
323 time after placing a predefined amount of PODS®-rhBDNF into a single well
324 of solution. The data collected appeared to fit the curve for Equation 2, which
325 describes the concentration of the intermediate product of two consecutive first
326 order reactions:

$$C_{rhBDNF} = C_{PODS} \cdot k_1 \cdot \left(\frac{e^{-k_1 \cdot t}}{k_2 - k_1} + \frac{e^{-k_2 \cdot t}}{k_1 - k_2} \right) \quad (2)$$

327 where C_{rhBDNF} is the concentration of rhBDNF and C_{PODS} is the concentra-
328 tion of PODS® [43].

329 We successfully fit the data to this equation's respective curve and empiri-
330 cally approximated k_1 to be $0.00686 (\frac{1}{hour})$ after plugging in our value for k_2
331 (See further detail in Supplementary Figure S7).

332 SDS-PAGE was used to separate PODS®-rhBDNF crystals into its con-
333 stituent proteins to determine the molar ratio of polyhedrin to rhBDNF. Vi-
334 sualization with Coomassie G-250 solution (Figure 6A) revealed three distinct
335 protein bands at 18.8 (a), 28.0 (b), and 46.8 (c) kDa, which correspond with
336 the molecular weights of H1-tagged BDNF monomer, polyhedrin, and H1-tagged
337 BDNF monomer attached with polyhedrin, respectively. Western blot analy-
338 sis was subsequently conducted to confirm the identity of the 18.8 kDa band
339 as rhBDNF. Enhanced chemiluminescence (Figure 6B) revealed four protein
340 bands at 14.0 (a), 18.8 (b), 37.6 (c), and 46.8 (d) kDa, which correspond with
341 the molecular weights of rhBDNF monomer, H1-tagged BDNF monomer, H1-
342 tagged BDNF dimer, and H1-tagged BDNF monomer attached with polyhedrin.
343 Immunoblot detection of the 18.8 kDa band further implicates its identity as
344 rhBDNF. SDS-PAGE images were converted to 8-bit grayscale and mean cor-
345 rected integrated pixel intensity values were calculated for protein bands located
346 at 28.0 and 18.8 kDa; the protein band detected at 46.8 kDa was omitted from

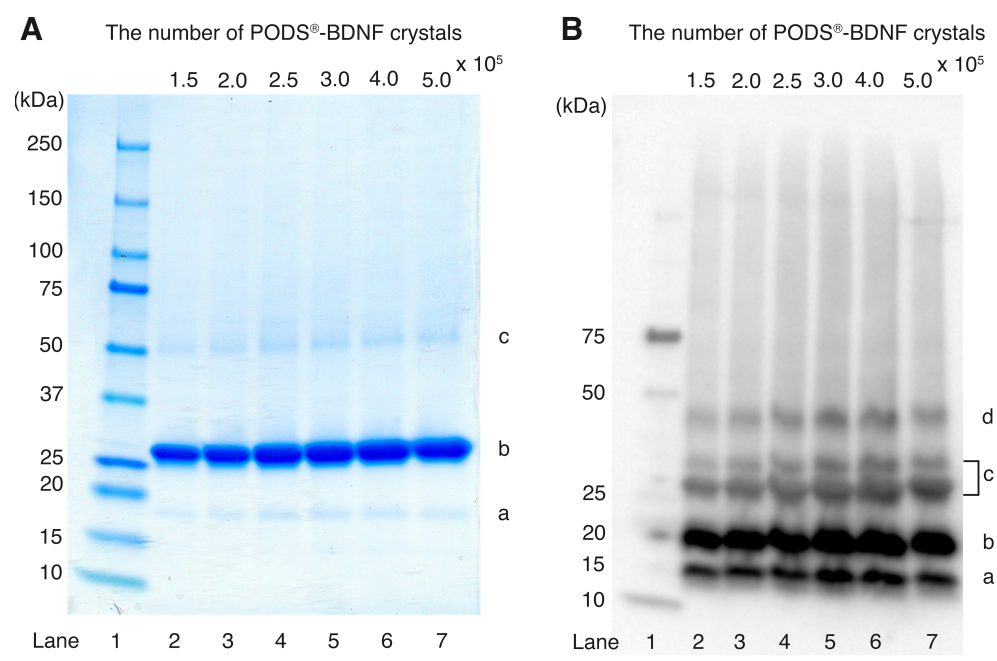
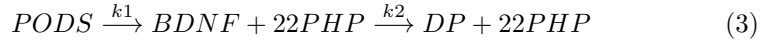


Figure 5: (A): SDS-PAGE analysis of PODS®-rhBDNF. Samples containing six quantities of PODS®-rhBDNF crystals were run on precast 4-15% polyacrylamide mini-gels and stained with Coomassie G-250 solution for visualization. Protein bands appear at approximately 18.8 (a), 28.0 (b), and 46.8 kDa (c). Lane 1: molecular weight marker. Lanes 2-7: samples containing

³⁴⁷ the final computation based on the fact that it contained a 1:1 ratio of poly-
³⁴⁸ hedrin to BDNF. Results indicate that the molecular ratio of polyhedrin to
³⁴⁹ rhBDNF is approximately 22:1. This transforms Equation (1) into:



³⁵⁰ Using these calculated rate constants with the calculated molar ratio, the
³⁵¹ resulting chemical gradient over time after PODS®-rhBDNF placement can be
³⁵² solved for any geometry by applying Fick's second Law of diffusion (Equation
³⁵³ 4) and the appropriate boundary (Equations 5 and 6) and initial conditions
³⁵⁴ (Equation 7):

$$\frac{dC}{dt} = \nabla \cdot (\nabla C \cdot D) - k_2 \cdot C \quad (4)$$

³⁵⁵ Boundary Conditions:

$$\delta C \Big|_{walls} = 0 \quad (5)$$

³⁵⁶ and

$$\delta C \Big|_{PODS} = k_1 \cdot PODS_0 \cdot e^{-k_1 \cdot t} \quad (6)$$

Initial conditions:

$$C \Big|_{t=0} = 0 \quad (7)$$

³⁵⁷ where C is the concentration of rhBDNF, D is diffusivity of rhBDNF (6.76
³⁵⁸ $\frac{mm^2}{day}$ [44]), $-k_2 \cdot C$ is the sink term corresponding to the degradation and cell-
³⁵⁹ utilization of the rhBDNF, and $PODS_0$ is the initial concentration of the cargo
³⁶⁰ protein (i.e., BDNF) within the PODS® crystals. The first boundary condition
³⁶¹ (Equation 4) shows that the concentrations of rhBDNF at the walls of the
³⁶² microfluidic device are fixed at 0. The second boundary condition (Equation 5)
³⁶³ represents the exponential nature of the decay of PODS®. Note that both are
³⁶⁴ Neumann boundary conditions.

365 We empirically tested two available microchannel lengths—(i.e., XonaTM-
366 XC150 [150 μm] and XonaTM-XC450 [450 μm]). This was done first because
367 mass (i.e., BDNF) transport from the neurotrophin compartment through the
368 micro-groove channels into the somal compartment is an important factor in
369 generating the concentration gradient *via* diffusion mixing. We determined that
370 the XonaTM Microfluidics XC450 was more appropriate for this study as the XC-
371 150's micro-groove channels were not long enough to generate the appropriate
372 concentration gradient throughout the somal compartment. This feature is rel-
373 evant to human inner ear because the micro-groove channels in the Xona device
374 simulates the presence of the osseous spiral lamina and modiolus between the
375 scala tympani and SGNs [41, 42]. Following device selection, we generated a
376 three-dimensional geometry mesh of the XC450 for the FEA (Figure 3B(d)).
377 Please see Supplementary Figure S6 for detailed measurements of the mesh.

378 The finite element model was then computed for different PODS[®]-rhBDNF
379 concentrations and time intervals to empirically optimize the rhBDNF concen-
380 tration gradient for hPSC-derived ONP differentiation into SGNs as well as
381 directed neurite extension. Figure 6 shows FEM-computed rhBDNF concen-
382 tration gradients for 20,000 PODS[®]-rhBDNF from Day 1–7. Note that the
383 rhBDNF concentrations were greater throughout D2–5 to promote the neuronal
384 differentiation and neurite outgrowth observed on D7 (Figure 6B). Computed
385 diffusion flux was uniform throughout D1–7 (Figure 6C). Also note that highest
386 concentration of rhBDNF released from PODS[®]-crystals was greater than 50
387 pg/mL, the concentration sufficient for otic neuronal differentiation and neurite
388 outgrowth of hPSC-derived ONP 3D spheroids determined in our previously
389 published data [9]. Optimization of the adequate number of PODS[®]-rhBDNF
390 was performed empirically; we also performed FEA with 10,000 and 40,000
391 PODS[®]-rhBDNF. Please see detailed discussion for the empirical optimization
392 in Supplementary Figure S8.

393 To objectively compare the degree of otic neuronal differentiation in the
394 hPSC-derived ONPs, we performed quantitative analysis of PAX8 and GATA3
395 double-positive cells using immunocytochemistry. We chose PAX8 and GATA3

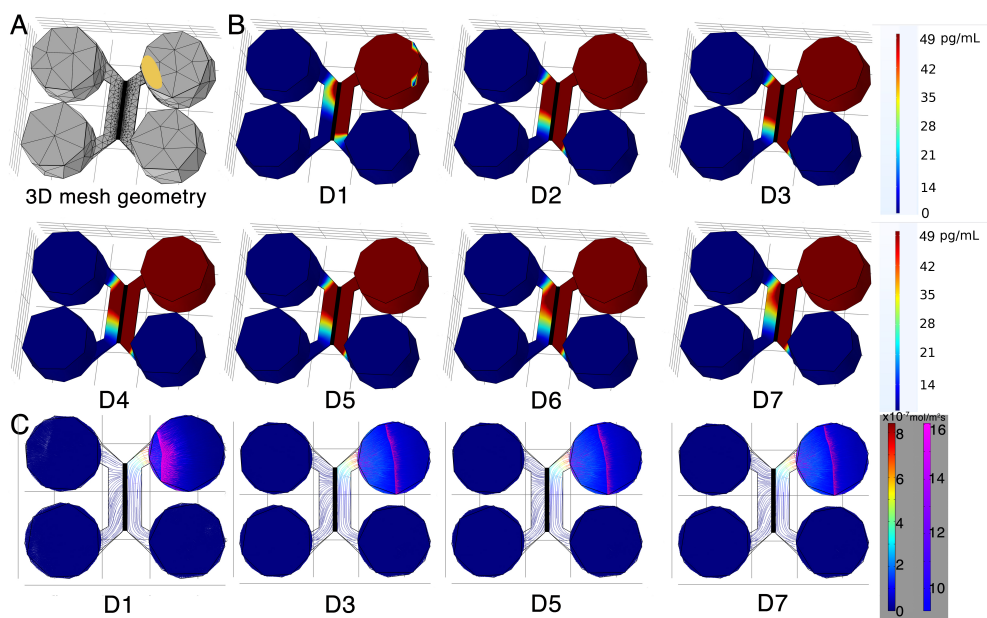


Figure 6: (A): 3D mesh geometry of a Xona™ XC450 created with Autodesk Inventor. A PODS®-rhBDNF ellipsoid disc is shown in yellow. (B): rhBDNF concentration gradient for 20,000 PODS®-rhBDNF from D1–D7. Note that the model does not account for media changes during the culture period. The corresponding color map shown has a range from 0 ng/mL to 49 pg/mL. (C): Diffusion flux ($\text{mol}/\text{m}^2\text{s}$) was computed using COMSOL Chemical Engineering module on D1, D3, D5, and D7.

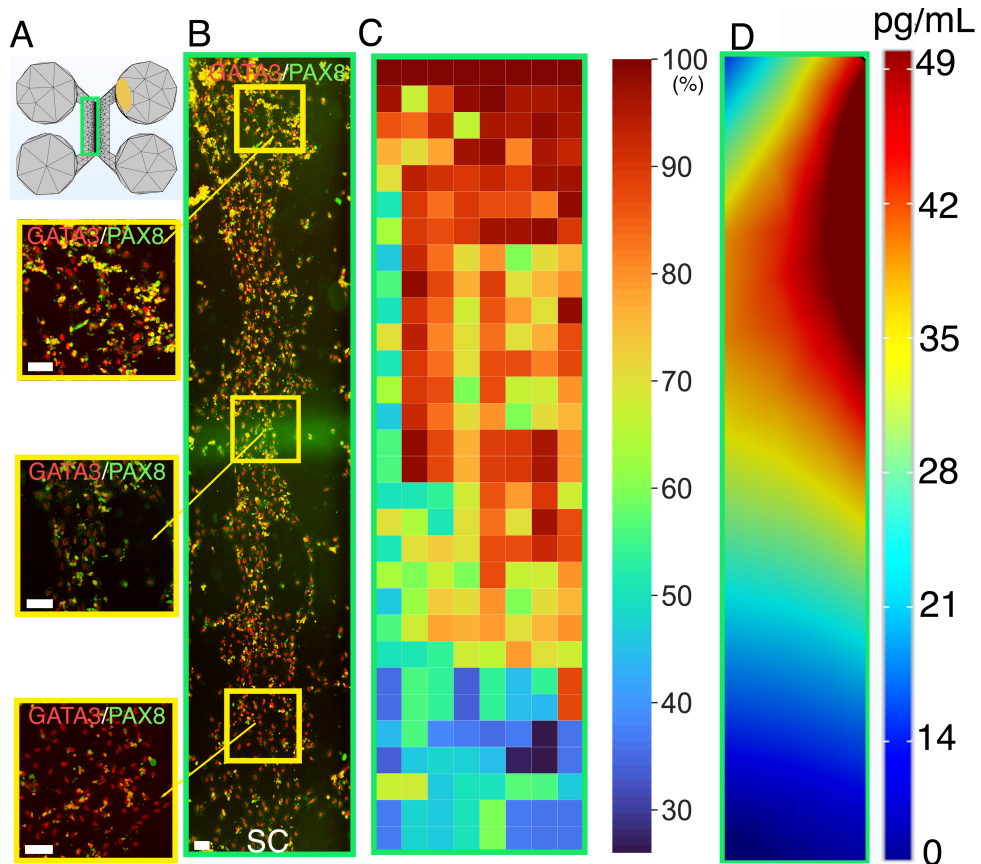


Figure 7: Human PSC-derived late-stage ONPs grown in a microfluidic device at Day 7 were stained for GATA3 (red) and PAX8 (green). (A): Geometry mesh of the microfluidic device Xona™ XC450 generated by Autodesk Inventor. The green square indicates the cell seeding location in the somal compartment of the device. An ellipsoid PODS®-rhBDNF disc is shown in yellow. (B): Cells were analyzed by staining with neuronal markers GATA3 (red) and PAX8 (green). Yellow highlighted regions are magnified on the left. SC: somal compartment. (C): Heat-map representation of double-positivity of hPSC-derived ONPs in the device for GATA3 and PAX8 ($n = 3$). Double-positivity increases from the lower to the upper portion of the somal compartment, suggesting that the higher BDNF concentration in the upper portion of the device improves differentiation. Scale bar: $100 \mu\text{m}$. (D): Prediction of BDNF concentration gradient released from PODS®-rhBDNF at seven days in culture using the finite element model. The corresponding color map is shown with a range from 0–49 pg/mL.

for this analysis because our previous studies indicated high expression of these protein markers in late-stage ONPs and early-stage SGNs [8, 9, 24]. Cells were stained in the somal compartment of the Xona™ device, highlighted in green in Figure 7A. Figure 7B shows the resulting image of cells in the somal compartment, and a heat-map representation of the percentage of double-positive cells is shown in Figure 7C. It should be noted here that the heat-map is sensitive to the differences in cell density across channel. This was accounted by averaging the double-positivity across three biological replicates. The heat-map indicates higher double-positivity in the upper region of the somal compartment, which is closest to the PODS®-rhBDNF disc placement (shown as an orange ellipse in Figure 7A) in the neurotrophin compartment. Double-positivity decreases in the somal compartment as distance from the PODS®-rhBDNF disc increases, supporting the presence of a rhBDNF neurotrophin gradient as predicted by our computational model (Figure 7D).

We defined two hypothetical directional angles to predict the orientation of hPSC-derived ONPs and neurite growth (Figure 8). The n -dimensional Euclidean space, denoted by \mathbb{R}^n , is a linear vector space in that we can use polar coordinates to compute the directionality of cells and neurites [45]. Here, we used $n = 1$ and 2 . For one-dimensional Euclidean space ($n = 1$), we simply drew a line for the Euclidean distance—the shortest distance between two points as shown in Figure 8A(b) (dark green lines). The two points were 1) the center point of the PODS®-rhBDNF disc (P) and 2) the mid point of the medial side (Q_{1-5}) (i.e., the near side to microgroove channels) of a pre-designated square (shown as a black square, zones 1–5 in Figure 8), respectively. The Euclidean distance angle (EDA), ϕ_i , was defined as the angle between the horizontal line zero direction and the line PQ_i that consists of the Euclidean distance where $i = 1 - 5$.

For two-dimensional Euclidean space ($n = 2$), we utilized Fick's first law, which dictates that the diffusion flux (D) is proportional to the concentration gradient (C) [46]. Based on this theorem, the direction of a flow vector can be used to represent the concentration gradient for directionality. We hypothesized

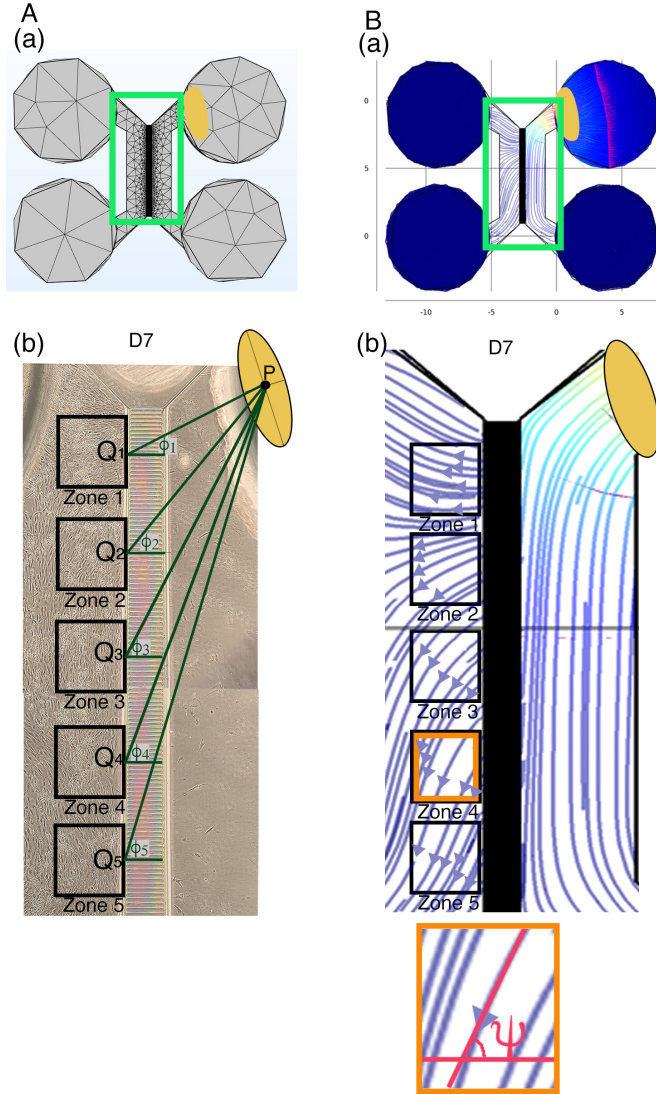


Figure 8: (A): Defining the Euclidean distance angle (EDA). (a) X-Y plane geometry mesh of a Xona™ XC450 device. Green square shows the area corresponding to the phase-contrast image below. An ellipsoid PODS®-rhBDNF disc is shown in yellow. (b) Yellow ellipse once again indicates the location of a disc containing PODS®-rhBDNF crystals (P: the center of this ellipse). In the somal compartment of the Xona™ XC450 device, we defined Zone 1–5, shown in black squares. A line was drawn from the center of the PODS®-rhBDNF disc (P) to (Q_{1-5}) (i.e., the near side to microgroove channels) of a pre-designated square (shown as a black square, zone 1–5) [i.e.,zone 1–5]). The Euclidean distance angle (EDA) for zone 1–5 was defined as ϕ_i , $i = 1–5$. (B): Defining diffusion flux angle (DFA). (a) Diffusion flux in the Xona™ XC450. Green squared area shows somal and neurotrophin compartments, which are magnified in (b). (b) Magnified image of diffusion flux of Zone 1–5 in the Xona™ XC450. Orange highlighted zone (zone 4) was highlighted at the bottom of (b), defining the DFA (ψ).

here that cell orientation is directionally controlled by the flux vector which is driven by the concentration gradient. Figure 8B shows the flow vectors in the somal compartment at Day 7 computed by the COMSOL Chemical Reaction Engineering module. We averaged the 10 flow vectors in each of five zones in Figure 8 to compute the diffusion flux angle (DFA), ψ_i , where $i = 1\text{--}5$ in Figure 8. To lighten the computational intensity, we reduced the dimension from 3D to 2D to compute diffusion flux. Please see justification in Supplementary Data. All of the computed EDAs and DFAs can be found in Supplementary Table 2.

Figure 9 shows time-series of microscopic phase-contrast photomicrographs obtained on Day 1, 3, and 7 in the five zones in the Xona™ XC450. Each preferred orientation of any given cell was computed and then plotted on a polar diagram (blue circle). Mean vector angle (MVA, shown in red line on Figure 9) and median vector angle were computed. All of the polar diagrams in Figure 9 show that preferred orientation of hPSC-derived ONPs distribute in an unimodal distribution. We also confirmed that a von Mises distribution is appropriate for these sets of data (See Supplementary Figure S9). We, therefore, then tested further to see if the cells had tendency to be oriented to a certain direction. To test this hypothesis, we used the Rayleigh test of uniformity to evaluate whether there is statistical evidence of circular directionality [32]. Computed p values for all the 15 conditions were less than 0.05, demonstrating that all of the conditions had statistically significant directionality. To further validate whether the observed angles have a tendency to cluster around the two hypothetical angles (i.e., EDA and DFA), we then performed the V test. Once again, p values for all 15 conditions were less than 0.05 except one (Zone 5 on Day 1), re-demonstrating that most of the conditions had statistically significant tendencies to cluster around the EDAs and DFAs. Additionally, we performed one sample test for the mean vector angle, which is similar to a one sample t-test on a linear scale. There was only one condition (Zone 1, day 1) that was statistically significant for EDA, whereas most of the conditions on Day 3 and 7 were statistically significant for DFA. Therefore, our results here demonstrated that hPSC-derived ONPs had greater tendency to cluster around DFA than

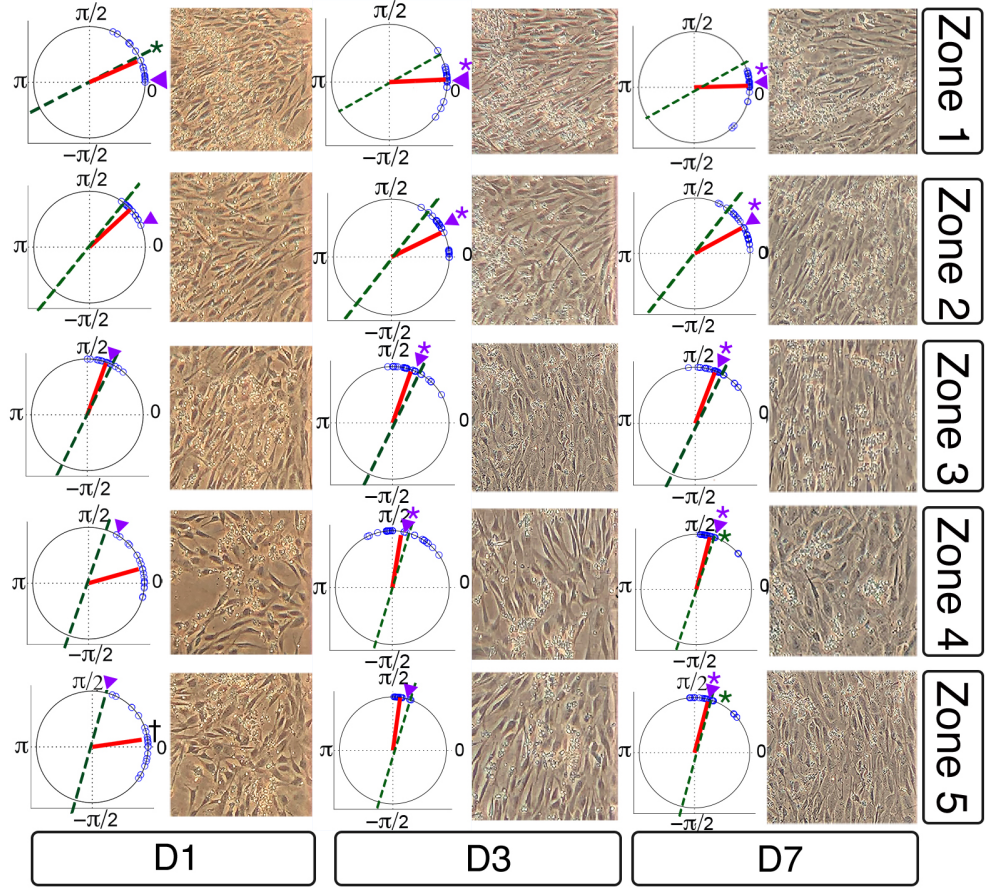


Figure 9: Preferred cell orientation analysis. Sequential phase-contrast images of the somal compartment of the Xona™ XC450 device in zones 1–5 (see Figure 8) on day 1 (D1), day 3 (D3), and day 7 (D7). A corresponding polar histogram indicates preferred orientation of hPSC-derived ONPs in an angle (0 – 2π radians) in blue circles. Mean vector angle is shown in red line. Green dotted line shows Euclidean Distance Angle (EDA) and purple triangle indicates Diffusion Flow Angle (DFA). † symbol indicates that p value > 0.01 . * symbol indicates that the mean vector angle fits within the 95% confidence internal ($\alpha < 0.05$).

458 EDA. All computed statistical values are shown in Supplementary Table S2.

459 To evaluate the direction of neurites of hPSC-derived ONPs, we first de-
460 fined EDA in Region 1-3 (ϕ'_j , $j = 1 - 3$) (Figure 10A) and DFA (ψ'_j , $j = 1 - 3$);
461 similarly defined ϕ_i and ψ_i as in Figure 8. All of the EDAs and DFAs defined
462 here can be found in Supplementary Table S3. Polar histograms of the neurite
463 direction angle in Regions 1–3 indicated that the two longest neurites were bi-
464 modal in nature (Figure 10B). In contrast, polar histograms of those cultured
465 with rhBDNF (negative control) and 800,000 PODS®-BNDF (positive control)
466 did not indicate bimodal distribution—the neurites did not show directionality
467 (Figure 10C). The Rayleigh test of uniformity for both the positive and negative
468 control were greater than 0.05, demonstrating that both of the conditions had
469 no statistically significant directionality (Supplementary Table S3: highlighted
470 in green). We also analyzed the direction of the neurites using circular statistics.
471 To obtain more realistic mean vector angles, we doubled each angle and reduced
472 the multiples modulo 360°. In circular statistics, the bimodal distributed data
473 can be transformed into a unimodal data by doubling the angle [32]. The mean
474 vector angles in Figure 10D (right column) indicates the situation where the
475 vectors were canceled out between the two groups of angles distributed in a bi-
476 modal fashion, resulting in inaccurate representation. A circular plot in Figure
477 10D (right column) showed doubled angles, representing actual representation
478 of the neurite vector angles. In all of the three regions, the Reyleigh test and V
479 test for EDA and DFA indicated directionality (Supplementary Table S3). One
480 sample test for the mean vector angles in Region 1–3 indicated that they were
481 not statistically different from DFA, but all of the three mean vector angles were
482 statistically different from EDA.

483 We also stained the devices for β -III tubulin to track neurite growth and
484 extension across the micro-groove channels as well as cell migration in three
485 selected regions (Figure 10A). The location of the PODS®-rhBDNF disc in
486 relation to the regions of interest in Figure 11A is indicated by a yellow cir-
487 cle. Quantitative analyses were performed and summarized in Figure 11B. Our
488 data indicate that neurite length is dependent on rhBDNF concentration, with

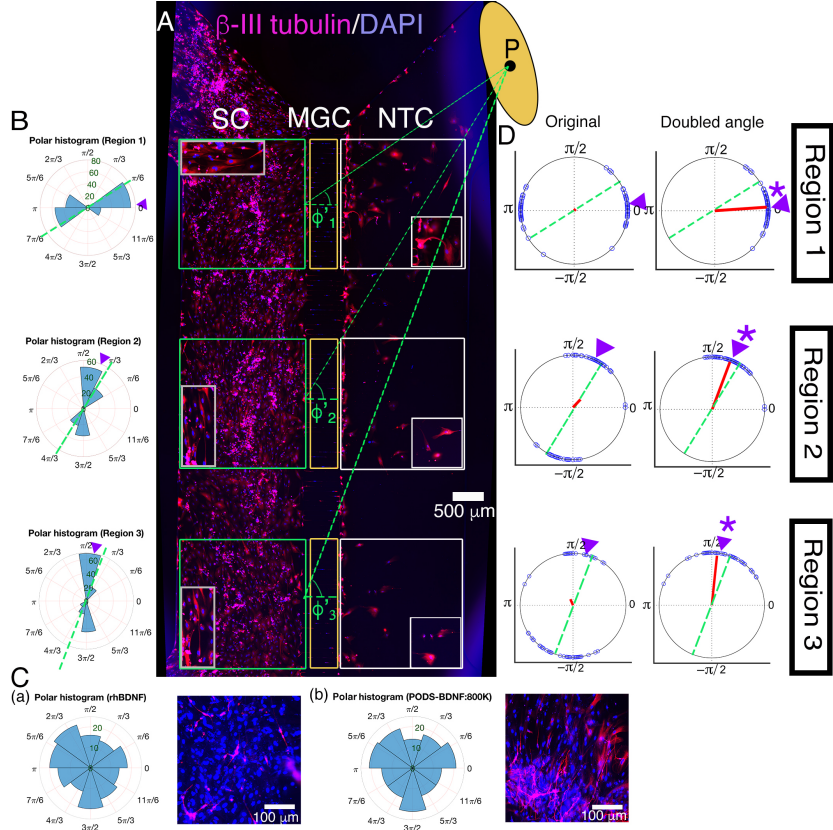


Figure 10: (A): Immunohistochemistry of hPSC-derived ONPs cultured in the Xona™ XC450 for seven days with β -III-Tubulin (pink fluorescence) and DAPI (blue fluorescence). A green line was drawn from the center of the BDNF disc (P) to the mid point of each of three pre-determined squares (Regions 1–3) in the somal compartment to define Euclidean Distance Angle (EDA: ϕ_i^i , $i = 1 - 3$). Green square: somal compartment (SC); yellow square: microgroove channels (MGC); white square: Neurotrophin compartment (NTC). High-power magnified images of the NTC and SC are shown. An ellipsoid PODS®-rhBDNF disc is shown in yellow. P: the center of the disc.(B): Polar histogram of neurite directional angles of hPSC-derived ONPs in the Xona™ XC450 at Day 7 (D7). The two longest neurites were measured. EDA: green dotted line. DFA: purple triangle. (C): (a) Right: Polar histogram of neurite directional angles of hPSC-derived ONPs cultured with 20 ng/mL of recombinant human BDNF for seven days. Left: Corresponding photomicrograph of immunocytochemistry with β -III tubulin (pink) and DAPI (blue). ()b) Right: Polar histogram of neurite directional angles of hPSC-derived ONPs cultured with 800,000 of PODS®-rhBDNF for seven days. Left: Corresponding photomicrograph of immunocytochemistry with β -III tubulin (pink) and DAPI (blue). (D): A circular plot of neurite directional angle of hPSC-derived ONPs in Region 1–3. Once again, the two longest neurites were plotted on a unit circle. Right column: Original directional angle distribution. Left column: the method of doubling the angle applied to the original data. Each datum point is shown as a blue circle. Mean vector angle is shown as a red line. Green dotted line shows Euclidean Distance Angle (EDA) and purple triangle indicates Diffusion Flow Angle (DFA). * symbol indicates that the mean vector angle fits within the 95% confidence internal ($\alpha < 0.05$.)

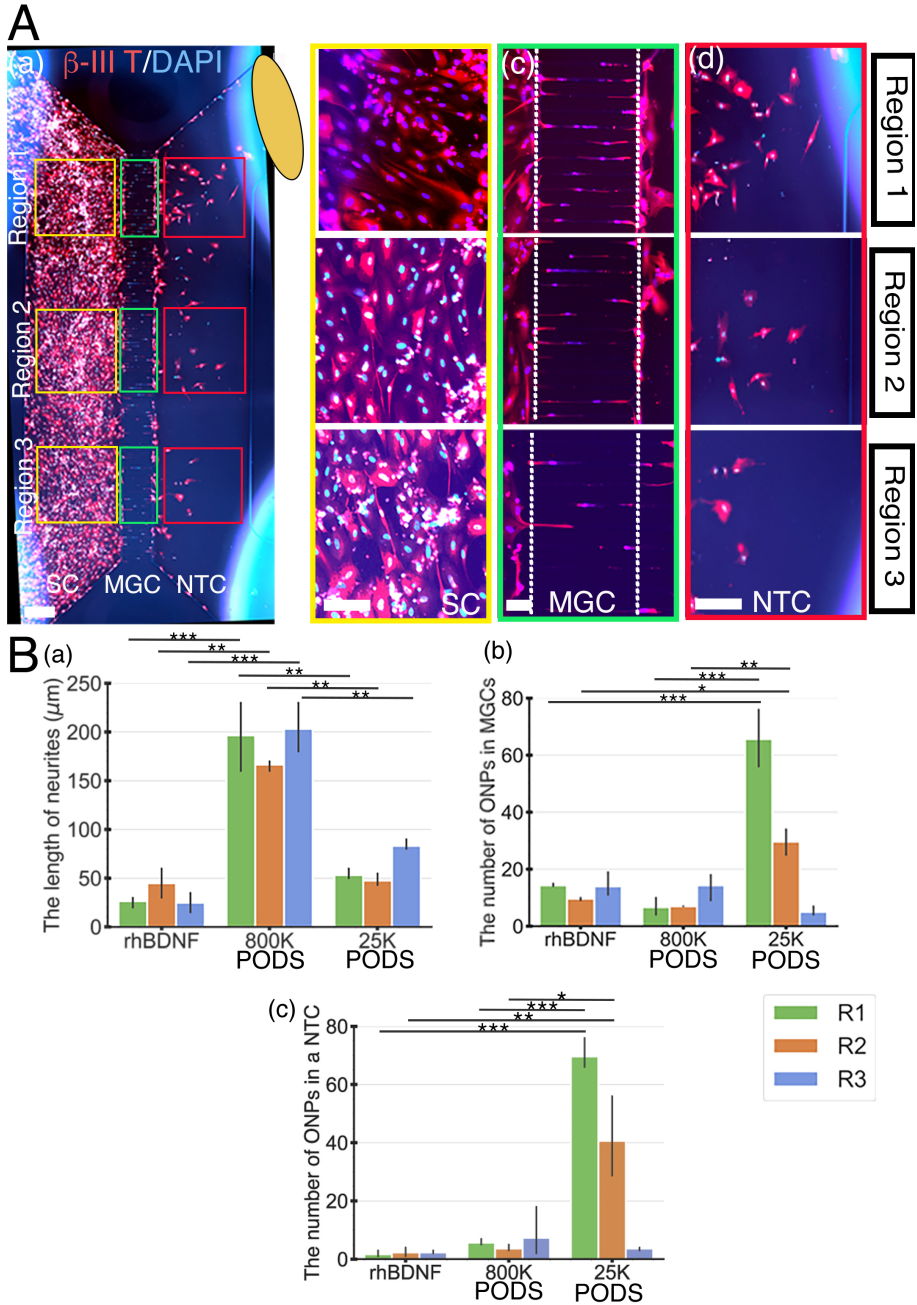


Figure 11: Human PSC-derived late-stage ONPs in the microfluidic device were stained with β -III tubulin (red) and DAPI (blue) to measure cell migration. (A): Late-stage ONPs stained after seven days in culture (a) with regions highlighted and magnified in the somal compartment (b), microgroove channels (c), and neurotrophin compartment (d). SC: somal compartment, MGC: microgroove channels, NTC: neurotrophic compartment. An ellipse-shaped PODS®-rhBDNF disc is shown in yellow. Scale bar (a): 500 μm ; (b)–(d): 100 μm . (B): Quantitative analyses of cell migration and neurite extension in devices using recombinant human BDNF, 800,000 PODS®-rhBDNF, or 20,000 PODS®-rhBDNF. * : $p < 0.05$, **: $p < 0.01$, ***: $p < 0.001$.

489 greater amounts of PODS[®]-rhBDNF promoting longer neurite growth (Figure
490 11B(a)). Lesser amounts of PODS[®]-rhBDNF, however, are necessary to cre-
491 ate an appropriate concentration gradient. In the presence of 20,000 PODS[®]-
492 rhBDNF, both neurite extension into the microchannels and cell migration into
493 the neurotrophin compartment are greatest in the region closest to the BDNF
494 source and decrease further from the PODS[®]-rhBDNF (Figure 11B(b,c)). Cell
495 migration is dependent on the distance from the source of BDNF, thus suggest-
496 ing the presence of a BDNF gradient as predicted by our model. Note that the
497 Xona microchannels intended to prevent from migration across channels.

498 **4. Discussion**

499 *4.1. Challenges of neurotrophin treatment in the inner ear*

500 This is a proof-of-concept study for the realization of a neurotrophic strip
501 to ascertain its scientific/technological parameters in a controlled *in vitro* en-
502 vironment. Neurotrophin gradients have been studied in multiple contexts
503 [47, 48, 49]. However, it has not been feasible to reliably provide, and maintain,
504 such a gradient to neurons *in vivo*, primarily because of technical challenges
505 including failure to provide a sustainable source and practical implantation.
506 Furthermore, while neurotrophin treatment has been recognized as a potential
507 treatment for sensorineural hearing loss, there has not been long-term clinical
508 success in this avenue to date. Most recent relevant clinical trials used adeno-
509 associated virus (AAV2) to deliver BDNF to the brain [50]. Although com-
510 pelling, this treatment does not attempt to precisely control the concentration
511 of BDNF, which could potentially interfere with normal functions in the target
512 organ [51]. Furthermore, this treatment may not be applicable to the inner ear,
513 as the procedure is MR-guided–technically infeasible in the inner ear. In this
514 study, we used PODS[®]-rhBDNF to generate and maintain a neurotrophic gra-
515 dient in a controlled manner. Our results indicate that 20,000 PODS-rhBDNF
516 allowed for a rhBDNF neurotrophin gradient such that hPSC-derived ONPs
517 survived, differentiated toward human SGNs, and also established directional

518 neurite outgrowth in a microfluidic device. Furthermore, our proposed solution
519 has greater potential to be translated into clinical practice; in addition to its
520 proven natural self-sustainability, we have shown previously that transplanta-
521 tion of PODS-rhBDNF is met with little immune rejection when embedded in
522 a nanofibrillar cellulose hydrogel in mice [9].

523 *4.2. Microfluidic device-generated gradient*

524 We utilized a microfluidic device to advance our understanding of direc-
525 tional neurite growth and otic neuronal differentiation in response to a rhBDNF
526 concentration gradient [52]. Among many *in vitro* concentration gradient sus-
527 taining culture devices, microfluidic devices have overcome many of the deficits
528 that conventional platforms (i.e., the Boyden chamber, Dunn chambers, or com-
529 partmentalized diffusion chambers) face [52]. Conventional platforms tend to
530 be sub-optimal in manipulating small volumes of fluid at the order of micro-
531 liters. Growth factors and proteins are used in minute amounts in our mi-
532 crofluidic device, and cultured stem cells are able to interact with endogenous
533 factors at biologically relevant concentrations. As mentioned earlier, this micro-
534 environment more accurately represents *in vivo* conditions. The Xona™ device
535 can be used to create and sustain a three-dimensional concentration gradient
536 over time (duration and diffusion profile dependent on the chemical kinetics
537 of the molecule) because of its microchannel array. The device limits convec-
538 tive flow in the gradient-forming areas by introducing microgroove channels
539 that generate high fluidic resistance, thereby limiting flow to diffusion. The
540 high resistance of the microchannel array also prolongs diffusion across them,
541 thereby increasing gradient formation and decreasing gradient steepness (essen-
542 tially elongating it). These features motivated us to generate a FEM, which
543 predicted the rhBDNF gradients associated with different numbers of PODS®-
544 BDNF crystals. Note, however, that this environment is geometrically different
545 from the micro-environment in the inner ear—a mesh geometry of the cochlea will
546 be needed to compute the PODS®-BDNF crystal number for implementation
547 in animals, as well as further clinical translation.

548 *4.3. Brain-derived neurotrophic factor*

549 Over the course of the past 20–30 years, it has been established that BDNF
550 mediates survival and differentiation activities of SGNs by binding and activating
551 tyrosine kinase receptor kinase B (TrkB), a member of the larger family of
552 Trk receptors [20]. Numerous studies have reported that BDNF can palliate
553 SGN degeneration in ototoxically deafened animals, a widely accepted model
554 for retrograde trans-synaptic SGN degeneration secondary to hair cell destruc-
555 tion [13, 14, 53, 54]. Additionally, it has been confirmed that there is a positive
556 correlation between SGN counts and CI performance [55]. It is then safe to
557 presume that BDNF application in CI recipients would enhance overall CI per-
558 formance, by preserving extant SGNs and their neurites. Although promising,
559 BDNF treatment in humans has not been implemented in the inner ear: simply
560 introducing BDNF into the inner ear poses significant hurdles.

561 Unsuccessful BDNF treatment is attributed to several factors [56]. The
562 blood half-life of BDNF protein is extremely short, lasting only 1–10 minutes
563 in plasma [57, 58] and one hour in CSF [59]. Due to BDNF’s high degradation
564 rate, treatment would require continuous replenishment, impractical in the clin-
565 ical setting. Furthermore, simply introducing BDNF in solution would presum-
566 ably promote non-directional neurite growth where directed neurite growth is
567 essential—especially in the case of our proposed bioactive CI. Directing neurite
568 growth towards the CI electrode array is pivotal in the ultimate goal of en-
569 hancing performance through the narrowing of the electrode-neuron gap. The
570 PODS® system can preclude this phenomena through its gradual release of
571 growth factor from a localized origin. This steady supply of BDNF from a lo-
572 calized origin not only generates a concentration gradient, but maintains it over
573 time. As shown in Figure 6, it is unmistakable that the slow-release nature of
574 PODS®-BDNF results in a concentration gradient over the course of Day 1–7.
575 As shown in Figures 7–11, careful calibration of the resulting BDNF gradient
576 can lead to the promotion of hPSC-derived ONP differentiation towards SGN
577 lineage and directed neurite extension.

578 It should be noted that our FEM assumes free diffusion of the rhBDNF

579 protein. In biological cell-culture conditions, rhBDNF released from PODS®-
580 rhBDNF has tendency to adhere to walls of the culture device, due to its nature
581 as a "sticky" protein of about 27 kDa (mature BDNF dimer) that is posi-
582 tively charged under physiological conditions (isoelectric point, pI = 9.4) [60].
583 As such, the physio-chemical properties of rhBDNF have rendered the protein
584 prone to diminished diffusive transport. This phenomenon was observed in pre-
585 liminary data where the ONPs failed to survive past 1–3 days of culture (data
586 not shown). To circumvent this issue we infused the culture media with a car-
587 rier protein (i.e., BSA), hypothesizing that the albumin would act as a carrier
588 for the released rhBDNF and allow for free diffusive transport throughout the
589 microfluidic device [61]. This hypothesis is supported by our sets of biolog-
590 ical validation data (Figures 7–11) clearly showing that hPSC-derived ONPs
591 responded to positively to the modification; they exhibited the expected cell
592 characteristics, body orientation, unidirectional neurite extension, and neurite
593 length. Note that as albumin is the single most highly concentrated protein
594 in the perilymph [62], therefore, an artificially introduced carrier protein would
595 not be required in future *in vivo* studies.

596 *4.4. Intracellular signaling initiated by the Tyrosine kinase B receptor*

597 Another issue for consideration in the interpretation of our results is the
598 intracellular cell-signaling mechanism elicited by rhBDNF. Human BDNF (ma-
599 ture dimeric form) binds with high affinity to the TrkB receptor. The binding
600 of BDNF to a TrkB receptor has been proven to have significance in the pro-
601 neuronal effects of BDNF [20]. Upon binding, TrkB dimerizes and activates
602 intrinsic kinase activities and other complex sets of intracellular signaling cas-
603 cades, beyond the scope of this study. However, it should be noted that activa-
604 tion also initiates internalization by endocytosis in the cellular membrane and
605 subsequently transported to the soma [63]. Therefore, the pro-neuronal effects
606 of rhBDNF in our results may be highly dependent on the status of the TrkB
607 receptors of the cell membrane of hPSC-derived ONPs. Our previous study
608 has demonstrated strong expression of TrkB receptors on derived ONPs [24],

609 however, more detailed studies on TrkB receptors of hPSC-derived ONPs and
610 SGNs are needed to deepen understanding.

611 *4.5. Degradation of PODS® crystals by protease activity*

612 In cell culture, degradation of PODS®-rhBDNF is likely due to the enzymatic
613 activity of cell-secreted proteases. The proteases break down the peptide
614 bonds of the encasing polyhedrin protein, creating openings in the structure to
615 allow release of the rhBDNF. Therefore, the presence of proteases is imperative
616 for the proper utilization of the PODS® technology. These proteases are
617 additionally responsible for subsequent degradation of the released rhBDNF.
618 Because cells were not present in the culture media used for the PODS® degra-
619 dation kinetics experiments, we infused the media with 10% FBS, which inher-
620 ently contains proteases, to promote polyhedrin degradation for BDNF release,
621 and subsequent BDNF degradation to acquire parameters that more accurately
622 describe *in vitro* events. Moreover, since the cells and PODS are initially segre-
623 gated into separate compartments within the culture device, cell-secreted pro-
624 teases are unlikely to reach and degrade the PODS in time to support ONP sur-
625 vival and differentiation, which was apparent in experiments conducted without
626 the addition of FBS (data not shown). Infusion of FBS was therefore required
627 in these experiments as well. For clinical translation, however, we presume that
628 cell-secreted proteases will be readily present in the inner ear and therefore
629 preclude the need for artificial supplementation.

630 *4.6. A concept design: Neurotrophic strip*

631 The plateau in CI performance in treatment of sensorineural hearing loss has
632 driven researchers to develop innovative supplementary treatment strategies to
633 push the field past this hurdle. Our approach strives to directly address the
634 issue at its core: the electrode-neuron gap, which can lead to serious implica-
635 tions include low spatial frequency resolution and high power consumption. We
636 can use our data as a launchpad for the neurotrophic strip (NS). The NS is a
637 biointerface concept that integrates an extended-release source of growth factor

638 to facilitate a protein gradient. Implanted in conjunction with the CI, it acts
639 as a bridge between the extant SGNs and implanted late-ONPs grown on the
640 electrode itself. The NS would promote survival of both cell populations, dif-
641 ferentiation of the late ONP implants, promote directional neurite growth and
642 synaptogenesis between the two, effectively creating a neuronal network between
643 the patient and the implanted CI. Each electrode would be able to stimulate cell
644 bodies at exceptionally high resolution, essential for greater intonation differ-
645 entiability (required for effective social interaction and music appreciation) and
646 so, increased quality of life for millions. Our successful outcomes are essential
647 to make a neurotrophic strip feasible in *in vivo* environment.

648 *4.7. The limitations of this study and future direction*

649 There are some limitations associated with this study. First, the reduction of
650 spacial dimension to 2D for diffusion modeling certainly affected the flux vector,
651 which determines the predicted concentration vector. Given that the thickness
652 (i.e., Z-axis) of the microfluidic device was 100 μm , we estimated that the effect
653 was minimal. In the future, we plan to use PSC-derived 3D spheroids in a somal
654 compartment so that flux vector and concentration gradient vector can more
655 accurately model the cell behavior. In this way, we will be able to circumvent
656 the need to reduce diffusion calculations to 2D for computation performance in
657 the modeling.

658 Secondly, we required to generate a model in that the BDNF's biological
659 transportation phenomenon from a PODS®-rhBDNF disc to a somal compart-
660 ment of a Xona™ device. Note that in this model, we focused on the major
661 dependent variable, BDNF concentration gradient to model the biological phe-
662 nomenon. Other physical variables to promote cell migration, otic neuronal
663 differentiation, and neurite growth were not take into consideration. These
664 variables include electotaxis (electrical potential), durotaxis (matrix's stiffness
665 [i.e., laminin 511 in our case]) [64], mechanotaxis (cell strain), and lastly cell
666 migration by random walk [65]. In our future study, we will take these vari-
667 ables into consideration to more accurately represent the migration and neurite

668 growth of hPSC-derived ONPs.

669 Insufficient contrast between cells and background in phase contrast images
670 led to inaccuracies in cell orientation computation for some images. To address
671 this issue, poor quality images were disregarded in the quantitative analysis.
672 We occasionally used manual measurement for accuracy. Our future study may
673 entail automated time-series cell analysis, which would allow more accurate
674 measurement. Also, another way to address this issue would be with a cell
675 membrane staining in the future.

676 While 20,000 of PODS[®]-rhBDNF were necessary for hPSC-derived ONPs
677 for otic neuronal differentiation and directional neurite outgrowth, this condition
678 may not be sufficient. For instance, it is still not known whether the effects
679 of other neurotrophic factors such as Neurotrophin-3 and Glial cell line-derived
680 neurotrophic factor could have a positive effect on ONP growth [20, 66, 67]. We
681 are planning to investigate these neurotrophic factors in the future. Other fac-
682 tors that could have an impact on directional neurite growth include endogenous
683 factors secreted from hPSC-derived ONPs. While our previous study demon-
684 strated that hPSC-derived ONPs only secreted negligible amount of BDNF that
685 were detected by ELISA [9], currently we do not have any data on other neu-
686 rotrophic factors or other molecules that could have affected directional neurite
687 growth in the inner ear. We chose BDNF first to study because the most inten-
688 sively studied neurotrophic factor in the field of hearing research is BDNF [20].
689 Previous studies have indicated that neurotrophic supports of SGNs are mainly
690 from BDNF and neurotrophin-3 (NT-3) [20, 60]. Therefore, the potential con-
691 founding effect of the secretions of other neurotrophic factors and molecules
692 secreted from derived SGNs are likely NT-3, for which further investigation is
693 necessary in the future.

694 Despite the aforementioned limitations associated in this study, the present
695 results generated BDNF concentration gradient, condition of which is necessary
696 for hPSC-derived ONPs to differentiate into the otic lineage (i.e., SGNs) and
697 also promoted directional neurite extension towards the POD-BDNF disc. The
698 technique will allow us to control neurite direction of transplanted hPSC-derived

699 ONPs in the inner ear. We will harness this method in our design of a bioactive
700 CI.

701 **Conclusions**

702 We were able to generate BDNF concentration gradient, enabling survival,
703 neuronal differentiation toward SGNs, and directed neurite extension of hPSC-
704 derived ONPs. The technique will allow us to control neurite direction of trans-
705 planted hPSC-derived ONPs in the inner ear. This proof-of-concept study pro-
706 vides a step toward next-generation bioacitve CI technology.

707 **Acknowledgment**

708 This work was supported by the American Otological Society Clinician Sci-
709 entist Award (AJM), the Triological Society/American College of Surgeons
710 Clinician Scientist Award (AJM), the Department of Otolaryngology of North-
711 western University (AJM), the NIH (NIDCD) K08 Clinician Scientist Award
712 K08DC13829-02 (AJM), and the Office of the Assistant Secretary of Defense of
713 Health Affairs through the Hearing Restoration Research Program (Award #:
714 RH170013:WU81XWUH-18-0712). Imaging work was performed at the North-
715 western University Center for Advanced Microscopy, which is generously sup-
716 ported by NCI CCSG P30 CA060553 awarded to the Robert H. Lurie Com-
717 prehensive Cancer Center, for which we thank Peter Dluhy, Constadina Ar-
718 vanitis, Ph.D., David Kirchenbuechler, Ph.D., and Wensheng (Wilson) Liu,
719 M.D. Some of microfluidic device experiments were performed in the Analytical
720 bioNanoTechnology (ANTEC) Core Facility of the Simpson Querrey Institute
721 at Northwestern University, which is supported by the Soft and Hybrid Nan-
722 otechnology Experimental (SHyNE) Resource (NSFECCS-1542205). We thank
723 Shreyas Bharadwaj (Cornell University), Kyle Coots (Midwestern University),
724 Andrew Oleksijew (the University of Nebraska), Duncan Chadly (California In-
725 stitute of Technology), and Shun Kobayashi (the University of Texas at Austin)

726 for their contribution to the earlier phases of this project. We thank Sara Dun-
727 lop (Department of Neurology, Northwestern University), and Dr. Jacqueline
728 Bond (the University of California San Diego) for assistance in Western Blot and
729 SDS-Page gels. We also thank Dr. Georgia Minakaki (Department of Neurol-
730 ogy, Northwestern University) on assistance in ELISA. Finally, our thanks and
731 appreciation go to our collaborator, Dr. Christian Pernstich (Cell Guidance
732 Systems), for continuous support and stimulating discussions on this project
733 since 2015.

734 **References**

- 735 [1] J. G. Naples, M. J. Ruckenstein, Cochlear Implant., Otolaryngologic Clinics
736 of North America 53 (1) (2020) 87–102. doi:10.1016/j.otc.2019.09.
737 004.
- 738 [2] B. S. Wilson, M. F. Dorman, Cochlear implants: A remarkable past
739 and a brilliant future, Hearing Research 242 (1-2) (2008) 3–21. arXiv:
740 NIHMS150003, doi:10.1016/j.heares.2008.06.005.
- 741 [3] C. Frick, M. Müller, U. Wank, A. Tropitzsch, B. Kramer, P. Senn, H. Rask-
742 Anderson, K. H. Wiesmüller, H. Löwenheim, Biofunctionalized peptide-
743 based hydrogels provide permissive scaffolds to attract neurite outgrowth
744 from spiral ganglion neurons, Colloids and Surfaces B: Biointerfaces 149
745 (2017) 105–114. doi:10.1016/j.colsurfb.2016.10.003.
- 746 [4] S. Hahnewald, A. Tscherter, E. Marconi, J. Streit, H. R. Widmer, C. Gar-
747 nham, H. Benav, M. Mueller, H. Löwenheim, M. Roccio, P. Senn, Response
748 profiles of murine spiral ganglion neurons on multi-electrode arrays., Jour-
749 nal of neural engineering 13 (1) (2016) 16011. doi:10.1088/1741-2560/
750 13/1/016011.
- 751 [5] R. K. Shepherd, S. Hatsushika, G. M. Clark, Electrical stimulation of
752 the auditory nerve: The effect of electrode position on neural excitation,

- 753 Hearing Research 66 (1) (1993) 108–120. doi:10.1016/0378-5955(93)
754 90265-3.
- 755 [6] M. Tykocinski, L. T. Cohen, B. C. Pyman, T. Roland, C. Treaba, J. Palamara,
756 M. C. Dahm, R. K. Shepherd, J. Xu, R. S. Cowan, N. L. Cohen,
757 G. M. Clark, Comparison of electrode position in the human cochlea using
758 various perimodiolar electrode arrays., The American journal of otology
759 21 (2) (2000) 205–211. doi:10.1016/S0196-0709(00)80010-1.
- 760 [7] A. Roemer, U. Köhl, O. Majdani, S. Klöß, C. Falk, S. Haumann, T. Lenarz,
761 A. Kral, A. Warnecke, Biohybrid cochlear implants in human neurosensory
762 restoration., Stem cell research and therapy 7 (1) (2016) 148. doi:10.
763 1186/s13287-016-0408-y.
- 764 [8] R. A. Heuer, K. T. Nella, H. T. Chang, K. S. Coots, A. M. Oleksijew,
765 C. B. Roque, L. H. Silva, T. L. McGuire, K. Homma, A. J. Matsuoka,
766 Three-dimensional otic neuronal progenitor spheroids derived from human
767 embryonic stem cells, *Tissue Engineering - Part A* 27 (3-4) (2021) 256–269.
768 doi:10.1089/ten.tea.2020.0078.
- 769 [9] H.-T. Chang, R. A. Heuer, A. M. Oleksijew, K. S. Coots, C. B. Roque, K. T.
770 Nella, T. L. McGuire, A. J. Matsuoka, An Engineered Three-Dimensional
771 Stem Cell Niche in the Inner Ear by Applying a Nanofibrillar Cellulose
772 Hydrogel with a Sustained-Release Neurotrophic Factor Delivery System,
773 *Acta Biomaterialia* 108 (2020) 111–127. doi:<https://doi.org/10.1016/j.actbio.2020.03.007>.
- 775 [10] L. Taylor, L. Jones, M. H. Tuszyński, A. Blesch, Neurotrophin-3 gradients
776 established by lentiviral gene delivery promote short-distance axonal bridg-
777 ing beyond cellular grafts in the injured spinal cord, *Journal of Neuroscience*
778 26 (38) (2006) 9713–9721. doi:10.1523/JNEUROSCI.0734-06.2006.
- 779 [11] P. Senn, M. Roccio, S. Hahnewald, C. Frick, M. Kwiatkowska, M. Ishikawa,
780 P. Bako, H. Li, F. Edin, W. Liu, H. Rask-Andersen, I. Pyykkö, J. Zou,

- 781 M. Mannerström, H. Keppner, A. Homsy, E. Laux, M. Llera, J. P. Lel-
782 louche, S. Ostrovsky, E. Banin, A. Gedanken, N. Perkas, U. Wank, K. H.
783 Wiesmüller, P. Mistrík, H. Benav, C. Garnham, C. Jolly, F. Gander, P. Ul-
784 rich, M. Müller, H. Löwenheim, NANOCI-Nanotechnology Based Cochlear
785 Implant with Gapless Interface to Auditory Neurons, *Otology and Neuro-*
786 *otology* 38 (8) (2017) e224—e231. doi:10.1097/MAO.0000000000001439.
- 787 [12] G. J. Goodhill, H. Baier, Axon Guidance: Stretching Gradients to
788 the Limit, *Neural Computation* 10 (3) (1998) 521–527. doi:10.1162/
789 089976698300017638.
- 790 [13] L. N. Gillespie, G. M. Clark, P. F. Bartlett, P. L. Marzella, BDNF-induced
791 survival of auditory neurons *in vivo*: Cessation of treatment leads to ac-
792 celerated loss of survival effects, *Journal of Neuroscience Research* 71 (6)
793 (2003) 785–790. doi:10.1002/jnr.10542.
- 794 [14] L. N. Pettingill, R. L. Minter, R. K. Shepherd, Schwann cells geneti-
795 cally modified to express neurotrophins promote spiral ganglion neuron
796 survival *in vitro*, *Neuroscience* 152 (3) (2008) 821–828. doi:10.1016/j.
797 *neuroscience*.2007.11.057.Schwann.
- 798 [15] R. K. Shepherd, A. Coco, S. B. Epp, Neurotrophins and electrical stim-
799 ulation for protection and repair of spiral ganglion neurons following
800 sensorineural hearing loss, *Hearing Research* 242 (2009) 100–109. doi:
801 10.1016/j.heares.2007.12.005.Neurotrophins.
- 802 [16] B. Baseri, J. J. Choi, T. Deffieux, G. Samiotaki, Y. S. Tung, O. Olu-
803 molade, S. A. Small, B. Morrison, E. E. Konofagou, Activation of sig-
804 naling pathways following localized delivery of systemically administered
805 neurotrophic factors across the bloodbrain barrier using focused ultra-
806 sound and microbubbles, *Physics in Medicine and Biology* 57 (7). doi:
807 10.1088/0031-9155/57/7/N65.
- 808 [17] K. Ikeda, S. Nagaoka, S. Winkler, K. Kotani, H. Yagi, K. Nakanishi,

- 809 S. Miyajima, J. Kobayashi, H. Mori, Molecular Characterization of Bom-
810 byx mori Cytoplasmic Polyhedrosis Virus Genome Segment 4, Journal of
811 Virology 75 (2) (2001) 988–995. doi:10.1128/jvi.75.2.988-995.2001.
- 812 [18] T. Suzuki, T. Kanaya, H. Okazaki, K. Ogawa, A. Usami, H. Watanabe,
813 K. Kadono-Okuda, M. Yamakawa, H. Sato, H. Mori, S. Takahashi, K. Oda,
814 Efficient protein production using a Bombyx mori nuclear polyhedrosis
815 virus lacking the cysteine proteinase gene, Journal of General Virology
816 78 (12) (1997) 3073–3080. doi:10.1099/0022-1317-78-12-3073.
- 817 [19] H. Mori, R. Ito, H. Nakazawa, M. Sumida, F. Matsubara, Y. Minobe,
818 Expression of Bombyx mori cytoplasmic polyhedrosis virus polyhedrin in
819 insect cells by using a baculovirus expression vector, and its assembly into
820 polyhedra, Journal of General Virology 74 (1) (1993) 99–102. doi:10.
821 1099/0022-1317-74-1-99.
- 822 [20] S. H. Green, E. Bailey, Q. Wang, R. L. Davis, The Trk A, B, C's of
823 Neurotrophins in the Cochlea., Anatomical record (Hoboken, N.J. : 2007)
824 295 (11) (2012) 1877–1895. doi:10.1002/ar.22587.
- 825 [21] I. Meyvantsson, D. J. Beebe, Cell culture models in microfluidic systems,
826 Annual Review of Analytical Chemistry 1 (1) (2008) 423–449. doi:10.
827 1146/annurev.anchem.1.031207.113042.
- 828 [22] Z.-J. Guo, M.-H. Yu, X.-Y. Dong, W.-L. Wang, T. Tian, X.-Y. Yu, X.-D.
829 Tang, Protein composition analysis of polyhedra matrix of Bombyx mori
830 nucleopolyhedrovirus (BmNPV) showed powerful capacity of polyhedra to
831 encapsulate foreign proteins., Scientific reports 7 (1) (2017) 8768. doi:
832 10.1038/s41598-017-08987-8.
- 833 [23] A. J. Matsuoka, Z. A. Sayed, N. Stephanopoulos, E. J. Berns, A. R. Wad-
834 hwani, Z. D. Morrissey, D. M. Chadly, S. Kobayashi, A. N. Edelbrock,
835 T. Mashimo, C. A. Miller, T. L. McGuire, S. I. Stupp, J. A. Kessler,
836 Creating a stem cell niche in the inner ear using self-assembling peptide

- 837 amphiphiles., Plos One 12 (12) (2017) e0190150. doi:10.1371/journal.
838 pone.0190150.
- 839 [24] A. J. Matsuoka, Z. D. Morrissey, C. Zhang, K. Homma, A. Belmadani,
840 C. A. Miller, D. M. Chadly, S. Kobayashi, A. N. Edelbrock, M. Tanaka-
841 Matakatsu, D. S. Whitlon, L. Lyass, T. L. McGruire, S. I. Stupp, J. A.
842 Kessler, Directed Differentiation of Human Embryonic Stem Cells Toward
843 Placode-Derived Spiral Ganglion-Like Sensory Neurons, Stem Cells Trans-
844 lational Medicine 6 (2017) 923–936. doi:10.1002/sctm.16-0032.
- 845 [25] H. Al-Ali, S. R. Beckerman, J. L. Bixby, V. P. Lemmon, In vitro models
846 of axon regeneration, Experimental Neurology 287 (Pt 3) (2017) 423–434.
847 doi:10.1016/j.expneurol.2016.01.020.
- 848 [26] U. K. Laemmli, Cleavage of structural proteins during the assembly of
849 the head of bacteriophage T4., Nature 227 (5259) (1970) 680–685. doi:
850 10.1038/227680a0.
- 851 [27] A. L. Mandel, H. Ozdener, V. Utermohlen, Identification of pro- and mature
852 brain-derived neurotrophic factor in human saliva., Archives of oral biology
853 54 (7) (2009) 689–695. doi:10.1016/j.archoralbio.2009.04.005.
- 854 [28] C. A. Schneider, W. S. Rasband, K. W. Eliceiri, NIH Image to ImageJ:
855 25 years of image analysis, Nature Methods 9 (7) (2012) 671–675. arXiv:
856 arXiv:1011.1669v3, doi:10.1038/nmeth.2089.
- 857 [29] R. W. Burry, Controls for immunocytochemistry: an update., The journal
858 of histochemistry and cytochemistry : official journal of the Histochemistry
859 Society 59 (1) (2011) 6–12. doi:10.1369/jhc.2010.956920.
- 860 [30] M. B. Mazalan, M. A. B. Ramlan, J. H. Shin, T. Ohashi, Effect of geomet-
861 ric curvature on collective cell migration in tortuous microchannel devices,
862 Micromachines 11 (7) (2020) 1–17. doi:10.3390/MI11070659.
- 863 [31] F. Xu, T. Beyazoglu, E. Hefner, U. A. Gurkan, U. Demirci, Automated
864 and adaptable quantification of cellular alignment from microscopic images

- 865 for tissue engineering applications, *Tissue Engineering - Part C: Methods*
866 17 (6) (2011) 641–649. doi:10.1089/ten.tec.2011.0038.
- 867 [32] E. Batschelet, *Circular Statistics in Biology (Mathematics in Biology Series)*,
868 1st Edition, Academic Press, New York, NY, 1981.
- 869 [33] P. Berens, M. J. Velasco, CircStat for Matlab: Toolbox for circular statistics
870 with Matlab, Max–Planck–Institut f ur biologische Kybernetik, Technical
871 Report No. 184 31 (10) (2009) 1–21. doi:doi:10.18637/jss.v031.i10.
- 872 [34] M. Pool, J. Thiemann, A. Bar-Or, A. E. Fournier, NeuriteTracer: A novel
873 ImageJ plugin for automated quantification of neurite outgrowth, *Journal*
874 of Neuroscience Methods 168 (1) (2008) 134–139. doi:10.1016/j.
875 jneumeth.2007.08.029.
- 876 [35] E. Meijering, M. Jacob, J.-C. F. Sarria, P. Steiner, H. Hirling, M. Unser,
877 Design and validation of a tool for neurite tracing and analysis in fluo-
878 rescence microscopy images., *Cytometry. Part A : the journal of the In-*
879 *ternational Society for Analytical Cytology* 58 (2) (2004) 167–176. doi:
880 10.1002/cyto.a.20022.
- 881 [36] M. Anniko, W. Arnold, T. Stigbrand, A. Strom, The Human Spiral Gan-
882 glion, *ORL* 57 (1995) 68–77.
- 883 [37] S. van der Walt, S. C. Colbert, G. Varoquaux, The NumPy Array: A
884 Structure for Efficient Numerical Computation, *Computing in Science En-*
885 *gineering* 13 (2) (2011) 22–30. doi:10.1109/MCSE.2011.37.
- 886 [38] J. D. Hunter, Matplotlib: A 2D Graphics Environment, *Computing in*
887 *Science Engineering* 9 (3) (2007) 90–95. doi:10.1109/MCSE.2007.55.
- 888 [39] P. Virtanen, R. Gommers, T. E. Oliphant, M. Haberland, T. Reddy,
889 D. Cournapeau, E. Burovski, P. Peterson, W. Weckesser, J. Bright, S. J.
890 van der Walt, M. Brett, J. Wilson, K. J. Millman, N. Mayorov, A. R. J.
891 Nelson, E. Jones, R. Kern, E. Larson, C. J. Carey, I. Polat, Y. Feng,

- 892 E. W. Moore, J. VanderPlas, D. Laxalde, J. Perktold, R. Cimrman, I. Hen-
893 riksen, E. A. Quintero, C. R. Harris, A. M. Archibald, A. H. Ribeiro,
894 F. Pedregosa, P. van Mulbregt, SciPy 1.0: fundamental algorithms for
895 scientific computing in Python., *Nature methods* 17 (3) (2020) 261–272.
896 doi:10.1038/s41592-019-0686-2.
- 897 [40] P. Berens, CircStat : A MATLAB Toolbox for Circular Statistics , *Journal*
898 *of Statistical Software* 31 (10). doi:10.18637/jss.v031.i10.
- 899 [41] M. Tuncel, H. S. Sürütü, K. M. Erbil, A. Konan, Formation of the cochlear
900 nerve in the modiolus of the guinea pig and human cochleae., *Archives of*
901 *medical research* 36 (5) (2005) 436–40. doi:10.1016/j.arcmed.2005.02.
902 003.
- 903 [42] B. Küçük, K. Abe, T. Ushiki, Y. Inuyama, S. Fukuda, Kazuo Ishikawa,
904 Microstructures of the Bony Modiolus in the Human Cochlea : A Scanning
905 Electron Microscopic Study, *Journal of Electron Microsc* 40 (40) (1991)
906 193–197.
- 907 [43] O. Levenspiel, *Chemical Reaction Engineering*, 3rd Edition, John Wiley
908 and Sons, Inc., New York, NY, 1999.
- 909 [44] M. Stroh, W. R. Zipfel, R. M. Williams, S. C. Ma, W. W. Webb, W. M.
910 Saltzman, Multiphoton microscopy guides neurotrophin modification with
911 poly(ethylene glycol) to enhance interstitial diffusion, *Nature Materials*
912 3 (7) (2004) 489–494. doi:10.1038/nmat1159.
- 913 [45] S. Axler, *Linear Algebra Done Right*, 3rd Edition, Springer Publishing,
914 New York, NY, 2015.
- 915 [46] J. Crank, *The mathematics of Diffusion*, 2nd Edition, Oxford University
916 Press, London, UK, 1979.
- 917 [47] K. M. Keefe, I. S. Sheikh, G. M. Smith, Targeting Neurotrophins to Specific
918 Populations of Neurons: NGF, BDNF, and NT-3 and Their Relevance

- 919 for Treatment of Spinal Cord Injury., International journal of molecular
920 sciences 18 (3). doi:10.3390/ijms18030548.
- 921 [48] B. I. Awad, M. A. Carmody, M. P. Steinmetz, Potential role of growth
922 factors in the management of spinal cord injury., World Neurosurgery 83 (1)
923 (2015) 120–131. doi:10.1016/j.wneu.2013.01.042.
- 924 [49] E. R. n. Hollis, M. H. Tuszyński, Neurotrophins: potential therapeutic tools
925 for the treatment of spinal cord injury., Neurotherapeutics : the journal of
926 the American Society for Experimental NeuroTherapeutics 8 (4) (2011)
927 694–703. doi:10.1007/s13311-011-0074-9.
- 928 [50] A. H. Nagahara, B. R. Wilson, I. Ivasyk, I. Kovacs, S. Rawalji, J. R.
929 Bringas, P. J. Piviroto, W. S. Sebastian, L. Samaranch, K. S. Bankiewicz,
930 M. H. Tuszyński, MR-guided delivery of AAV2-BDNF into the entorhi-
931 nal cortex of non-human primates., Gene therapy 25 (2) (2018) 104–114.
932 doi:10.1038/s41434-018-0010-2.
- 933 [51] S. D. Croll, C. Suri, D. L. Compton, M. V. Simmons, G. D. Yan-
934 copoulos, R. M. Lindsay, S. J. Wiegand, J. S. Rudge, H. E. Scharfman,
935 Brain-derived neurotrophic factor transgenic mice exhibit passive avoid-
936 ance deficits, increased seizure severity and in vitro hyperexcitability in
937 the hippocampus and entorhinal cortex., Neuroscience 93 (4) (1999) 1491–
938 1506. doi:10.1016/s0306-4522(99)00296-1.
- 939 [52] A. Dravid, S. Parittotokkaporn, Z. Aqrawe, S. J. O'Carroll, D. Svirskis,
940 Determining Neurotrophin Gradients in Vitro to Direct Axonal Outgrowth
941 following Spinal Cord Injury, ACS Chemical Neuroscience 11 (2) (2020)
942 121–132. doi:10.1021/acschemneuro.9b00565.
- 943 [53] T. Yamagata, J. M. Miller, M. Ulfendahl, N. P. Olivius, R. A. Altschuler,
944 I. Pyykkö, G. Bredberg, Delayed neurotrophic treatment preserves nerve
945 survival and electrophysiological responsiveness in neomycin-deafened
946 guinea pigs., Journal of neuroscience research 78 (1) (2004) 75–86. doi:
947 10.1002/jnr.20239.

- 948 [54] M. P. Zanin, M. Hellstr??m, R. K. Shepherd, A. R. Harvey, L. N. Gillespie,
949 Development of a cell-based treatment for long-term neurotrophin expres-
950 sion and spiral ganglion neuron survival, *Neuroscience* 277 (2014) 690–699.
951 [doi:10.1016/j.neuroscience.2014.07.044](https://doi.org/10.1016/j.neuroscience.2014.07.044).
- 952 [55] M. Seyyedi, L. Viana, J. J. Nadol, Within-subject comparison of word
953 recognition and spiral ganglion cell count in bilateral cochlear implant
954 recipients, *Otol Neurotol* 35 (8) (2014) 1446–1450. [doi:10.1097/MAO.000000000000443](https://doi.org/10.1097/MAO.000000000000443).Within-Subject.
- 955 [56] A. Henriques, C. Pitzer, A. Schneider, Neurotrophic growth factors for the
956 treatment of amyotrophic lateral sclerosis: where do we stand?, *Frontiers*
957 in neuroscience 4 (2010) 32. [doi:10.3389/fnins.2010.00032](https://doi.org/10.3389/fnins.2010.00032).
- 958 [57] J. F. Poduslo, G. L. Curran, Permeability at the blood-brain and
959 blood-nerve barriers of the neurotrophic factors: NGF, CNTF, NT-3,
960 BDNF, *Molecular Brain Research* 36 (2) (1996) 280–286. [doi:10.1016/0169-328X\(95\)00250-V](https://doi.org/10.1016/0169-328X(95)00250-V).
- 961 [58] T. Sakane, W. M. Pardridge, Carboxyl-directed pegylation of brain-derived
962 neurotrophic factor markedly reduces systemic clearance with minimal loss
963 of biologic activity (1997). [doi:10.1023/A:1012117815460](https://doi.org/10.1023/A:1012117815460).
- 964 [59] R. G. Soderquist, E. D. Milligan, E. M. Sloane, J. A. Harrison, K. K.
965 Douvas, J. M. Potter, T. S. Hughes, R. A. Chavez, K. Johnson, L. R.
966 Watkins, M. J. Mahoney, PEGylation of brain-derived neurotrophic factor
967 for preserved biological activity and enhanced spinal cord distribution.,
968 *Journal of biomedical materials research. Part A* 91 (3) (2009) 719–729.
969 [doi:10.1002/jbm.a.32254](https://doi.org/10.1002/jbm.a.32254).
- 970 [60] M. Sasi, B. Vignoli, M. Canossa, R. Blum, Neurobiology of local and inter-
971 cellular BDNF signaling, *Pflugers Archiv : European journal of physiology*
972 469 (5-6) (2017) 593–610. [doi:10.1007/s00424-017-1964-4](https://doi.org/10.1007/s00424-017-1964-4).

- 975 [61] X. Li, Y. Su, S. Liu, L. Tan, X. Mo, S. Ramakrishna, Encapsulation
976 of proteins in poly(l-lactide-co-caprolactone) fibers by emulsion electro-
977 spinning, *Colloids and Surfaces B: Biointerfaces* 75 (2) (2010) 418–424.
978 [doi:10.1016/j.colsurfb.2009.09.014](https://doi.org/10.1016/j.colsurfb.2009.09.014).
- 979 [62] E. E. L. Swan, M. Peppi, Z. Chen, K. M. Green, J. E. Evans, M. J.
980 McKenna, M. J. Mescher, S. G. Kujawa, W. F. Sewell, Proteomics analysis
981 of perilymph and cerebrospinal fluid in mouse., *The Laryngoscope* 119 (5)
982 (2009) 953–958. [doi:10.1002/lary.20209](https://doi.org/10.1002/lary.20209).
- 983 [63] T. Numakawa, S. Suzuki, E. Kumamaru, N. Adachi, M. Richards,
984 H. Kunugi, BDNF function and intracellular signaling in neurons, *Histology
985 and Histopathology* 25 (2) (2010) 237–258. [doi:10.14670/HH-25.237](https://doi.org/10.14670/HH-25.237).
- 986 [64] C. Gentile, Engineering of Spheroids for Stem Cell Technology, *Cur-
987 rent Stem Cell Research & Therapy* 11 (2016) 652–665. [doi:10.2174/1574888x10666151001114848](https://doi.org/10.2174/1574888x10666151001114848).
- 988 [65] H. Berg, *Random Walks in Biology*, Princeton Universtiyl Press, Prinston,
989 NJ, 1983.
- 990 [66] H. Li, F. Edin, H. Hayashi, O. Gudjonsson, N. Danckwardt-Lillies, H. En-
991 gqvist, H. Rask-Andersen, W. Xia, Guided growth of auditory neurons:
992 Bioactive particles towards gapless neural electrode interface, *Biomaterials*
993 122 (2017) 1–9. [doi:10.1016/j.biomaterials.2016.12.020](https://doi.org/10.1016/j.biomaterials.2016.12.020).
- 994 [67] J. Schulze, H. Staeker, D. Wedekind, T. Lenarz, A. Warnecke, Expression
995 pattern of brain-derived neurotrophic factor and its associated receptors:
996 Implications for exogenous neurotrophin application., *Hearing Research* 413
997 (2020) 108098. [doi:10.1016/j.heares.2020.108098](https://doi.org/10.1016/j.heares.2020.108098).